Equatorial circular motion in Kerr spacetime

Daniela Pugliese,[1,2,3,*] Hernando Quevedo,[1,2,4,†] and Remo Ruffini[1,2,‡]

[1]*Dipartimento di Fisica, Università di Roma La Sapienza, Piazzale Aldo Moro 5, I-00185 Roma, Italy*
[2]*ICRANet, Piazzale della Repubblica 10, I-65122 Pescara, Italy*
[3]*School of Mathematical Sciences, Queen Mary, University of London, Mile End Road, London E1 4NS, United Kingdom*
[4]*Instituto de Ciencias Nucleares, Universidad Nacional Autónoma de México, AP 70543, México, DF 04510, Mexico*

We analyze the properties of circular orbits of test particles on the equatorial plane of a rotating central mass whose gravitational field is described by the Kerr spacetime. For rotating black holes and naked singularities we explore all the spatial regions where circular orbits can exist and analyze the behavior of the energy and the angular momentum of the corresponding test particles. In particular, we find all the radii at which a test particle can have zero angular momentum due to the repulsive gravity effects generated by naked singularities. We classify all the stability zones of circular orbits. It is shown that the geometric structure of the stability zones of black holes is completely different from that of naked singularities.

I. INTRODUCTION

The Kerr spacetime describes the exterior gravitational field of a rotating mass M with specific angular momentum $a = J/M$, where J is the total angular momentum of the gravitational source. In Boyer-Lindquist coordinates, the Kerr metric has the form

$$ds^2 = dt^2 - \frac{\rho^2}{\Delta} dr^2 - \rho^2 d\theta^2 - (r^2 + a^2)\sin^2\theta d\phi^2$$
$$- \frac{2M}{\rho^2} r(dt - a\sin^2\theta d\phi)^2, \tag{1}$$

where

$$\Delta \equiv r^2 - 2Mr + a^2, \quad \text{and} \quad \rho^2 \equiv r^2 + a^2\cos^2\theta. \tag{2}$$

This metric is an axisymmetric, stationary (nonstatic), asymptotically flat solution of Einstein equations in vacuum. The redshift infinity surface and event horizons are described, respectively, by the equations

$$g_{tt} = 0, \qquad g^{rr} = 0. \tag{3}$$

Then, the solutions of these equations are, respectively,

$$r_{\pm}^0 = M \pm \sqrt{M^2 - a^2\cos^2\theta}, \quad \text{and}$$
$$r_{\pm} = M \pm \sqrt{M^2 - a^2}. \tag{4}$$

Considering that $\theta \in [0, \pi]$, the radii $r_{\pm}^0$ and $r_{\pm}$ exist when $|a| \leq M$ (Kerr black hole); in particular, for $|a| = M$ (extreme Kerr black hole) the two horizons coincide, $r_+ = r_- = M$. The outer static limit is r_+^0; it corresponds to the outer boundary of the ergosphere.

*d.pugliese.physics@gmail.com
†quevedo@nucleares.unam.mx
‡ruffini@icra.it

A naked singularity case occurs when $|a| > M$ (for more details about the Kerr metric, see, for instance, [1–7]).

The most important limiting cases are the Schwarzschild metric which is recovered for $a = 0$, and the Minkowski metric of special relativity for $a = M = 0$. The Kerr metric in Boyer-Lindquist coordinates is singular when $\rho = 0$ and when $\Delta = 0$. However, a calculation of the Kretschmann curvature scalar reveals that a true curvature singularity occurs only for $\rho = 0$. Therefore, the surface represented by $r = 0$ and $\theta = \pi/2$ corresponds to an intrinsic curvature singularity [1,2,8,9].

In previous works [10–12], the motion of test particles along circular orbits around static, spherically symmetric spacetimes was investigated in detail. We are now interested in studying the more general case of stationary, axisymmetric spacetimes. The study of the circular motion around compact objects is of particular interest in the context of astrophysics. Indeed, an infinitesimal thin disk of test particles traveling in circular orbits can be considered as an idealized model for an accretion disk of matter surrounding the central body. Such an idealized model could be used, for instance, to estimate the amount of energy released by matter being accreted by the central mass [13]. In addition, one can ask the question whether this hypothetical accretion disk carries information about the nature of the central compact object. In a recent work [10–12], this question was answered positively. Indeed, we found that the geometric structure of the infinitesimal thin disk around a Reissner-Nordström compact object strongly depends on the mass-to-charge ratio.

In the present work, we generalize our previous analysis and study the motion of test particles along circular orbits on the equatorial plane of the Kerr spacetime. We are especially interested in studying the differences between the gravitational field of black holes and naked singularities. Test particles moving along circular orbits are

particularly appropriate to measure the effects generated by naked singularities. For the sake of simplicity, we limit ourselves to the case of equatorial trajectories because they are confined in the equatorial geodesic plane. This is a consequence of the fact that the Kerr solution is invariant under reflections with respect to the equatorial plane. Nonequatorial geodesics present an additional difficulty because the corresponding planes are not geodesic. This case will not be considered in the present work.

This paper is organized as follows. In Sec. II, we use the formalism of the effective potential to derive the conditions for the existence of circular orbits on the equatorial plane of the Kerr spacetime. Section III is devoted to the study of circular orbits around a rotating black hole. In Sec. IV, we investigate the case of naked singularities and find all the regions where circular orbits are allowed. We analyze in detail the values of the energy and the angular momentum as well as the stability properties of the test particles for all the allowed regions in black holes and naked singularities. In Sec. IV D, we present a summary of behavior of the radii that determine the distribution of test particles around the central body, and of the radii of the last stable circular orbits. Finally, in Sec. V we discuss our results.

II. CIRCULAR ORBITS

We consider the circular motion of a test particle of mass μ in the background represented by the Kerr metric (1). We limit ourselves to the case of orbits situated on the equatorial plane only which are defined by means of the conditions

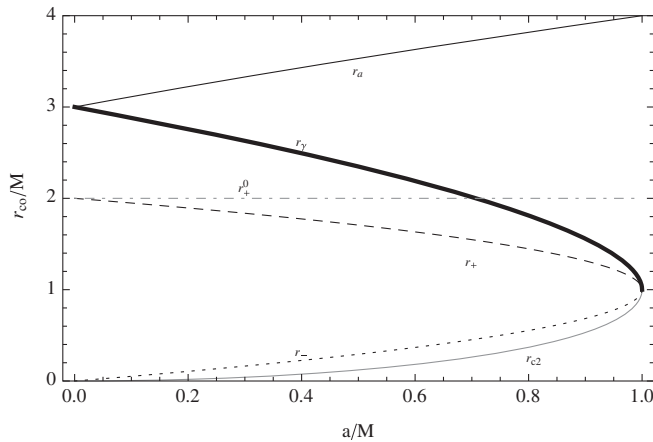$$\theta = \pi/2, \quad \text{and} \quad \frac{d\theta}{d\tau} = 0, \tag{5}$$

FIG. 1. The outer horizon r_+ (dashed curve), the inner horizon r_- (dotted curve), and r_a (solid thin black curve), r_{c2} (solid gray curve), and r_γ (solid thick black curve) are plotted as a function of the black hole intrinsic angular momentum a/M. The dash-dotted gray line represents the outer boundary of the ergosphere $r_+^0 = 2M$.
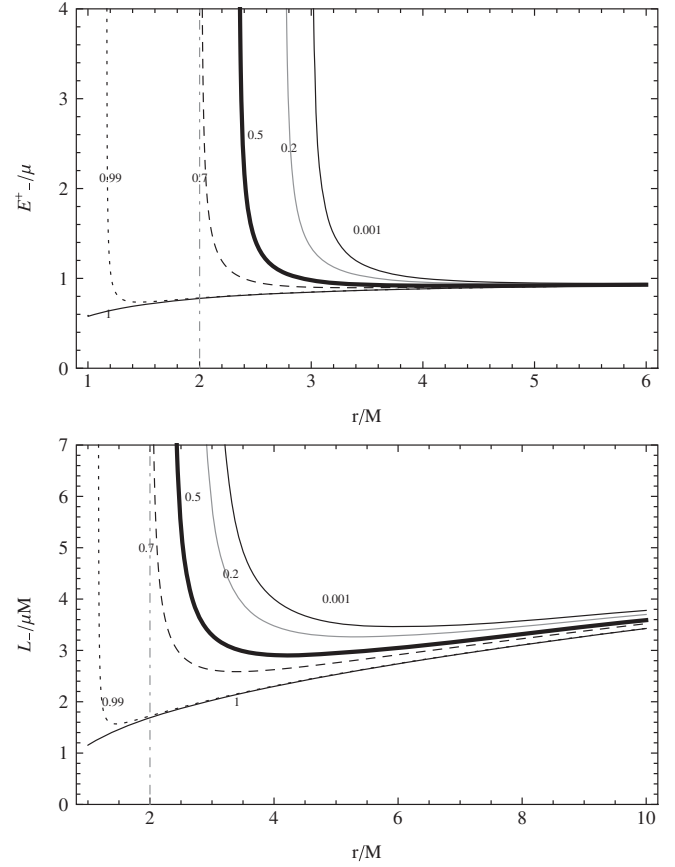

FIG. 2. The energy $E^{(+)} \equiv E(L_-)$ (upper plot) and the angular momentum L_- (bottom plot) of circular orbits in a rotating Kerr black hole with angular momentum $0 < a \leq M$, for selected values of a/M in the interval $r > r_\gamma$. For $a \neq M$ the energy $E^{(+)}$ is always positive and diverges as r approaches r_γ. The dash-dotted gray line represents the outer boundary of the ergosphere $r_+^0 = 2M$.

where τ is the particle's proper time. We note that for $\theta = \pi/2$ the outer boundary of the ergosphere Eq. (4) is $r_+^0 = 2M$ while $r_-^0 = 0$.

The tangent vector u^a to a curve $x^\alpha(\tau)$ is $u^\alpha = dx^\alpha/d\tau = \dot{x}^\alpha$. The momentum $p^\alpha = \mu \dot{x}^\alpha$ of a particle with mass μ can be normalized so that $g_{\alpha\beta}\dot{x}^\alpha\dot{x}^\beta = -k$, where $k = 0, 1, -1$ for null, spacelike, and timelike curves, respectively.

Since the metric is independent of ϕ and t, the covariant components p_ϕ and p_t of the particle's four-momentum are conserved along its geodesic. Thus, we use the fact that the quantity

$$E \equiv -g_{\alpha\beta}\xi_t^\alpha p^\beta \tag{6}$$

is a constant of motion, where $\xi_t = \partial_t$ is the Killing field representing stationarity. In general, we may interpret E, for timelike geodesics, as representing the total energy of the test particle for a particle coming from radial infinity, as measured by a static observer at infinity. On the other hand,
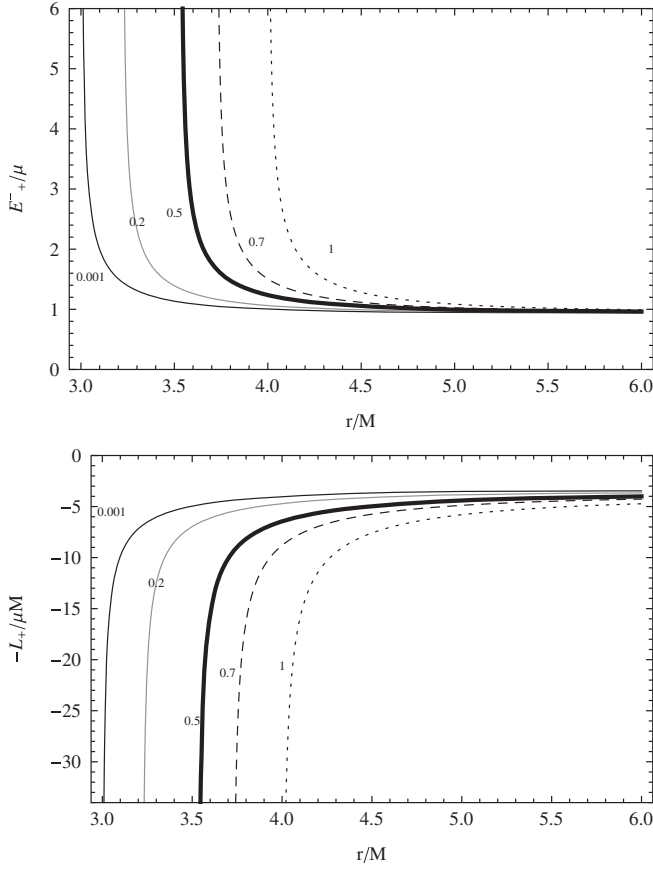
FIG. 3. The energy $E_+^{(-)} \equiv E(-L_+)$ and angular momentum $L = -L_+$ of circular orbits in a Kerr black hole with angular momentum $0 < a \leq M$, for selected values of a/M in the region $r > r_a$. The energy $E_+^{(-)}$ is always positive and diverges as r approaches r_a.

the rotational Killing field $\xi_\phi = \partial_\phi$ yields the following constant of motion:

$$L \equiv g_{\alpha\beta}\xi_\phi^\alpha p^\beta. \tag{7}$$

We interpret L as the angular momentum of the particle.

In this work, we analyze circular orbits involving a potential function $V(r)$. It represents that value of E/μ that makes r into a "turning point" ($V = E/\mu$), in other words, that value of E/μ at which the (radial) kinetic energy of the particle vanishes [14]. The (positive) effective potential is

$$V = -\frac{B}{2A} + \frac{\sqrt{B^2 - 4AC}}{2A}, \tag{8}$$

where [1–3,8,9]

$$A \equiv (r^2 + a^2)^2 - a^2\Delta, \tag{9}$$

$$B \equiv -2aL(r^2 + a^2 - \Delta), \tag{10}$$

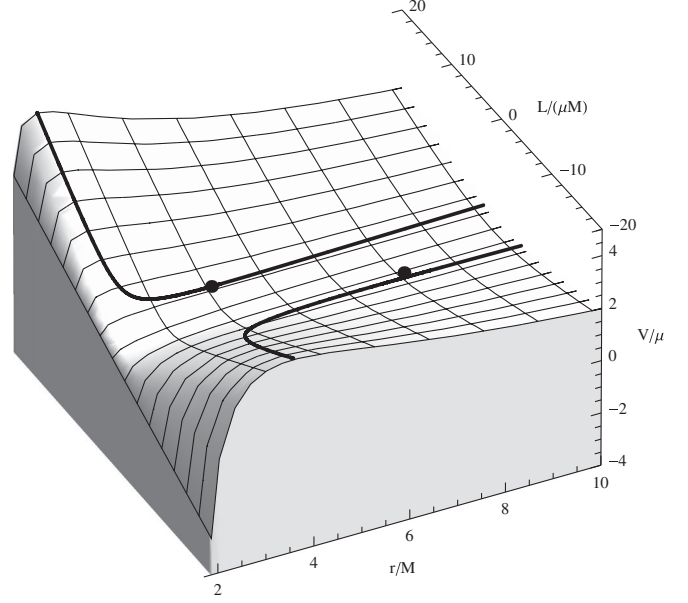$$C \equiv a^2L^2 - (M^2r^2 + L^2)\Delta. \tag{11}$$

FIG. 4. The effective potential V/μ for a neutral particle of mass μ in a Kerr black hole with $a/M = 0.5$ is plotted as a function of r/M in the range [1.71, 10] for the radial coordinate and in the range $[-10, 10]$ for the angular momentum $L/(\mu M)$. The outer horizon is situated at $r_+ = (1 + 1/\sqrt{2})M$ (see text). Circular orbits exist for $r > 2[1 + \sin(\pi/18)]M \approx 2.347M$. The solid curve represents the location of circular orbits (stable and unstable). Stable (unstable) circular orbits are minima (maxima) of the effective potential function. The last stable circular orbits are represented by a point. The minima are located at $r = 4.233M$ with $L = 2.903/(M\mu)$ and $E = 0.918\mu$, and at $r = 7.554M$ with $L = -3.884/(M\mu)$ and $E = 0.955\mu$.
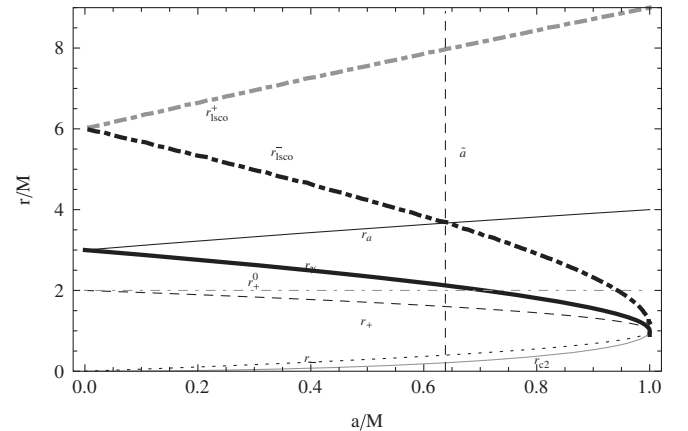

FIG. 5. The outer horizon r_+ (dashed curve), the inner horizon r_- (dotted curve), and r_a (solid thin black curve), r_{c2} (solid gray curve), r_γ (solid thick black curve), last stable circular orbits r_{lsco}^+ (thick dash-dotted black curve) and r_{lsco}^- (thick dash-dotted gray curve) are plotted as functions of the black hole intrinsic angular momentum a/M. The curves r_{lsco}^+ and r_{lsco}^- represent the radius of the last stable circular orbit for particles with angular momentum $-L_+$ and L_-, respectively. Circular orbits with $L = L_-$ exist for $r/M > r_\gamma$ and with $L = -L_+$ for $r > r_a$. The line $\tilde{a} \approx 0.638\,285M$ is also plotted. The thin dash-dotted gray line represents the outer boundary of the ergosphere $r_+^0 = 2M$.
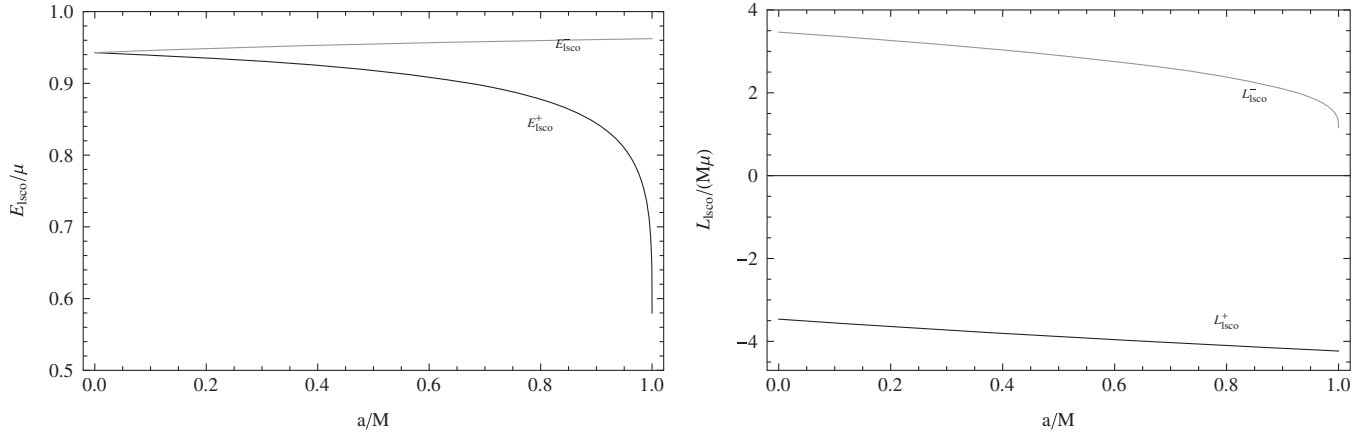
FIG. 6.   The energy E_{lsco}/μ and the angular momentum $L_{\mathrm{lsco}}^{\pm}/(M\mu)$ of the last stable circular orbit as functions of the ratio $a/M \le 1$ of a Kerr black hole.

The negative solution of the effective potential equation

$$V^- \equiv -\frac{B}{2A} - \frac{\sqrt{B^2 - 4AC}}{2A} \qquad (12)$$

can be studied by using the following symmetry:

$$V(L) = -V^-(-L). \qquad (13)$$

We can note that the potential function (8) is invariant under the mutual transformation $a \to -a$ and $L \to -L$. Therefore, we will limit our analysis to the case of positive values of a for corotating $(L > 0)$ and counterrotating orbits $(L < 0)$.

The investigation of the motion of test particles in the spacetime (1) is thus reduced to the study of motion in the effective potential V. We will focus on (timelike) circular orbits for which (see also [15])

$$\dot{r} = 0, \qquad V = E/\mu, \qquad \partial V/\partial r = 0. \qquad (14)$$

TABLE I.   Classification of circular orbits of test particles in a Kerr black hole. Here $\tilde{a} \approx 0.638\,285M$. For each region we present the value of the orbital angular momentum and the stability property.

Region	Angular momentum	Stability
	Case: $0 < a < M$	
$]r_\gamma, r_a]$	L_-	r_{lsco}^-
$]r_a, \infty[$	$-L_+(L_-)$	$r_{\mathrm{lsco}}^+(r_{\mathrm{lsco}}^-)$
	$0 < a < \tilde{a}(r_a < r_{\mathrm{lsco}}^-)$	
$]r_\gamma, r_a[$	L_-	Unstable
$]r_a, r_{\mathrm{lsco}}^-[$	$(L_-, -L_+)$	Unstable
$]r_{\mathrm{lsco}}^-, r_{\mathrm{lsco}}^+[$	$L_-(-L_+)$	Stable (Unstable)
$]r_{\mathrm{lsco}}^+, \infty[$	$(L_-, -L_+)$	Stable
	$\tilde{a} \le a < M(r_a \le r_{\mathrm{lsco}}^-)$	
$]r_\gamma, r_{\mathrm{lsco}}^-[$	L_-	Unstable
$]r_{\mathrm{lsco}}^-, r_a[$	L_-	Stable
$]r_a, r_{\mathrm{lsco}}^+[$	$L_-(-L_+)$	Stable (Unstable)
$]r_{\mathrm{lsco}}^+, \infty[$	$(L_-, -L_+)$	Stable

Moreover, we use the following notation for the angular momentum solutions

$$\frac{L_\pm}{\mu M} \equiv \frac{|\frac{a^2}{M^2} \pm 2\frac{a}{M}\sqrt{\frac{r}{M}} + \frac{r^2}{M^2}|}{\sqrt{\frac{r^2}{M^2}(\frac{r}{M} - 3) \mp 2\frac{a}{M}\sqrt{\frac{r^3}{M^3}}}}, \qquad (15)$$

and the corresponding energies

$$\frac{E_\pm^{(+)}}{\mu} \equiv \frac{E(L_\pm)}{\mu}$$

$$= \frac{\frac{(r^5 M)^{1/4}[[a^2 + (r-2M)r](a \mp \sqrt{(r^3)/(M))})]}{\sqrt{(r-3M)\sqrt{\frac{r}{M}\mp 2a}}} + 2arL_\pm}{r[r^3 + a^2(r + 2M)]}, \qquad (16)$$

and

$$\frac{E_\pm^{(-)}}{\mu} \equiv \frac{E(-L_\pm)}{\mu}$$

$$= \frac{\frac{(r^5 M)^{1/4}[[a^2 + (r-2M)r](a \mp \sqrt{(r^3)/(M))})]}{\sqrt{(r-3M)\sqrt{\frac{r}{M}\mp 2a}}} - 2arL_\pm}{r[r^3 + a^2(r + 2M)]}, \qquad (17)$$

respectively. The investigation of the above expressions for the angular momentum and energy of the test particle for different values of the radial coordinate allows us to extract physical information about the behavior of the gravitational source. We mention for an analysis of the test particle motion in Kerr spacetime, for example, [16–37].

III. BLACK HOLES

In this section we shall consider the black hole case $0 < a \le M$. In the nonextreme black hole case $(0 < a < M)$, it is $g_{tt} > 0$ for $0 < r < r_-^0$ and $r > r_+^0$. Inside the interval $r_-^0 < r < r_+^0$ the metric component g_{tt} changes its sign. Moreover, g_{tt} vanishes for $r = r_\pm^0$ and $0 < \cos^2\theta \le 1$, and also at $r = 2M$ for $\theta = \pi/2$. The location of these hypersurfaces is such that $r_-^0 < r_- < r_+ < r_+^0$.

The region $r_-^0 < r < r_+^0$, where $g_{tt} < 0$, is called *ergo-region*. In this region the Killing vector $\xi_t^a = (1, 0, 0, 0)$ becomes spacelike or $g_{ab}\xi_t^a\xi_t^b = g_{tt} < 0$. This fact implies, in particular, that a static observer, i.e., an observer with four velocity proportional to ξ_t^a so that $\dot\theta = \dot r = \dot\phi = 0$, cannot exist inside the ergoregion; an observer inside this region is forced to move.

For the extreme black hole case ($a = M$) it holds $r_- = r_+ = M$. Then, $g_{tt} > 0$ for $0 < r < r_-^0$ and $r > r_+^0$ when $0 \leq \cos^2\theta < 1$, and for $0 < r < M$ and $r > M$ when $\cos^2\theta = 1$; moreover, $g_{tt} = 0$ at $r = r_\pm^0$ in the interval $0 \leq \cos^2\theta < 1$, and at $r = M$ for $\cos^2\theta = 1$. The location of the special radii is such that $r_-^0 < r_- = r_+ < r_+^0$ for $0 \leq \cos^2\theta < 1$ and $r_-^0 = r_- = r_+ = r_+^0$ for $\cos^2\theta = 1$.

To investigate the solutions of the conditions of circular motion given by Eq. (14) it is convenient to introduce the following radii:

$$r_a \equiv 4M \cos\left[\frac{1}{6}\arccos\left[-1 + 2\frac{a^2}{M^2}\right]\right]^2, \qquad (18)$$

$$r_{c2} \equiv 4M \sin\left[\frac{1}{6}\arccos\left[1 - 2\frac{a^2}{M^2}\right]\right]^2, \qquad (19)$$

$$r_\gamma \equiv 2M\left(1 + \sin\left[\frac{1}{3}\arcsin\left[1 - 2\frac{a^2}{M^2}\right]\right]\right), \qquad (20)$$

which have the two limiting cases

$$r_a = r_\gamma = 3M, \qquad r_{c2} = 0 \quad \text{for } a = 0, \qquad (21)$$

and

$$r_a = 4M, \qquad r_{c2} = r_\gamma = M \quad \text{for } a = M. \qquad (22)$$

The dependence of these radii on the specific angular momentum is shown in Fig. 1. It is then possible to show that circular orbits can exist only for $r > r_\gamma$ and that there are two regions with different values for the angular momentum, namely,

$$r_\gamma < r \leq r_a, \quad \text{where } L = L_-, \qquad (23)$$

and

$$r > r_a, \quad \text{where } L = -L_+, \quad \text{and} \quad L = L_-. \qquad (24)$$

Moreover, in the extreme black hole case, $a = M$, the circular orbits are situated at

$$r = r_a = 4M, \qquad (25)$$

with two different possible values for the angular momentum:

$$L = \frac{13}{4\sqrt{2}}M\mu \quad \text{with} \quad E = \frac{5}{4\sqrt{2}}\mu, \quad \text{and}$$

$$L = -\frac{13}{4\sqrt{2}}M\mu \quad \text{with} \quad E = \frac{149}{140\sqrt{2}}\mu. \qquad (26)$$

As for the first interval $r_\gamma < r \leq r_a$, the behavior of the corresponding energy and angular momentum is illustrated in Fig. 2. First we note that the area covered by this region increases as the specific angular momentum of the black hole increases. Whereas r_a and r_γ coincide and equal $3M$ for nonrotating black holes ($a = 0$), their maximum separation is reached in the case of extreme black holes ($a = M$) for which r_γ coincides with the outer horizon
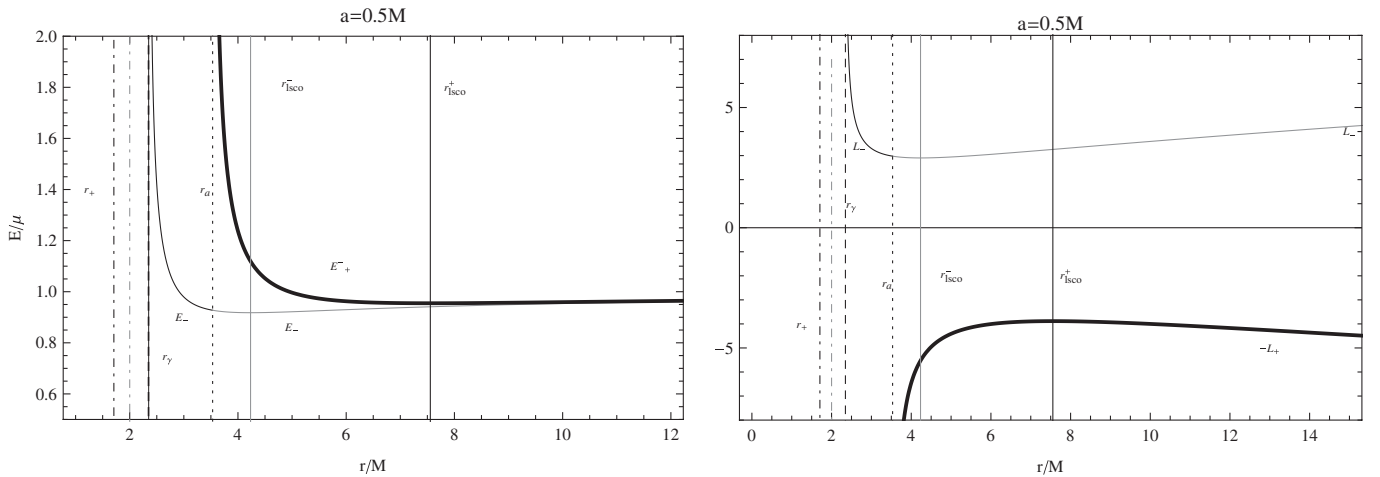
FIG. 7.   The energy E/μ (left plot) and the angular momentum $L/(\mu M)$ (right plot) of circular orbits in a Kerr black hole with $a = 0.5M$ as functions of the radial coordinate r/M. The energy $E_+^{(-)} \equiv E(-L_+)$ and the angular momentum $-L_+$ are represented by thick solid black curves, and the energy $E_-^{(+)} \equiv E(L_-)$ and the angular momentum L_- by thin solid black curves. In $r_\gamma < r < r_a$ there are unstable circular orbits with L_-. For $r_a < r < r_{\rm lsco}^-$ there are unstable circular orbits with L_- and $-L_+$. For $r_{\rm lsco}^- < r < r_{\rm lsco}^+$ there are stable circular orbits with L_- and unstable with $-L_+$. Finally for $r > r_{\rm lsco}^+$ there are stable circular orbits with L_- and $-L_+$. The radii $r_+ = 1.707\,11M$, $r_\gamma = 2.3473M$, $r_a = 3.532\,09M$ and $r_{\rm lsco}^- = 4.233M$, and $r_{\rm lsco}^+ = 7.554\,58M$ are also plotted. It is evident that $E(-L_+) > E(L_-)$. The dash-dotted gray line represents the outer boundary of the ergosphere $r_+^0 = 2M$.

radius. In the region $r > r_a$, circular orbits are allowed with different values of the angular momentum (the particular case with $L = -L_+$ is illustrated in Fig. 3).

We see that in the gravitational field of a black hole with $0 < a < M$, particles with angular momentum $L = L_-$ can exist in the entire region $r > r_\gamma$. As the radius r_γ is approached, the angular momentum L_- and the corresponding energy $E_-^{(+)} = E(L_-)$ diverge, indicating that the hypersurface $r = r_\gamma$ is lightlike, i.e., it is the limiting orbit for timelike particles with $L = L_-$. Moreover, particles with angular momentum $L = -L_+$ can move

along circular orbits in the interval $r > r_a$, and the limiting lightlike counterrotating orbit corresponds to $r = r_a$ where both L_+ and the energy $E_+^{(-)} = E(-L_+)$ diverge.

Stability

From the physical viewpoint it is important to find the minimum radius for stable circular orbits which is determined by the inflection points of the effective potential function, i.e., by the condition
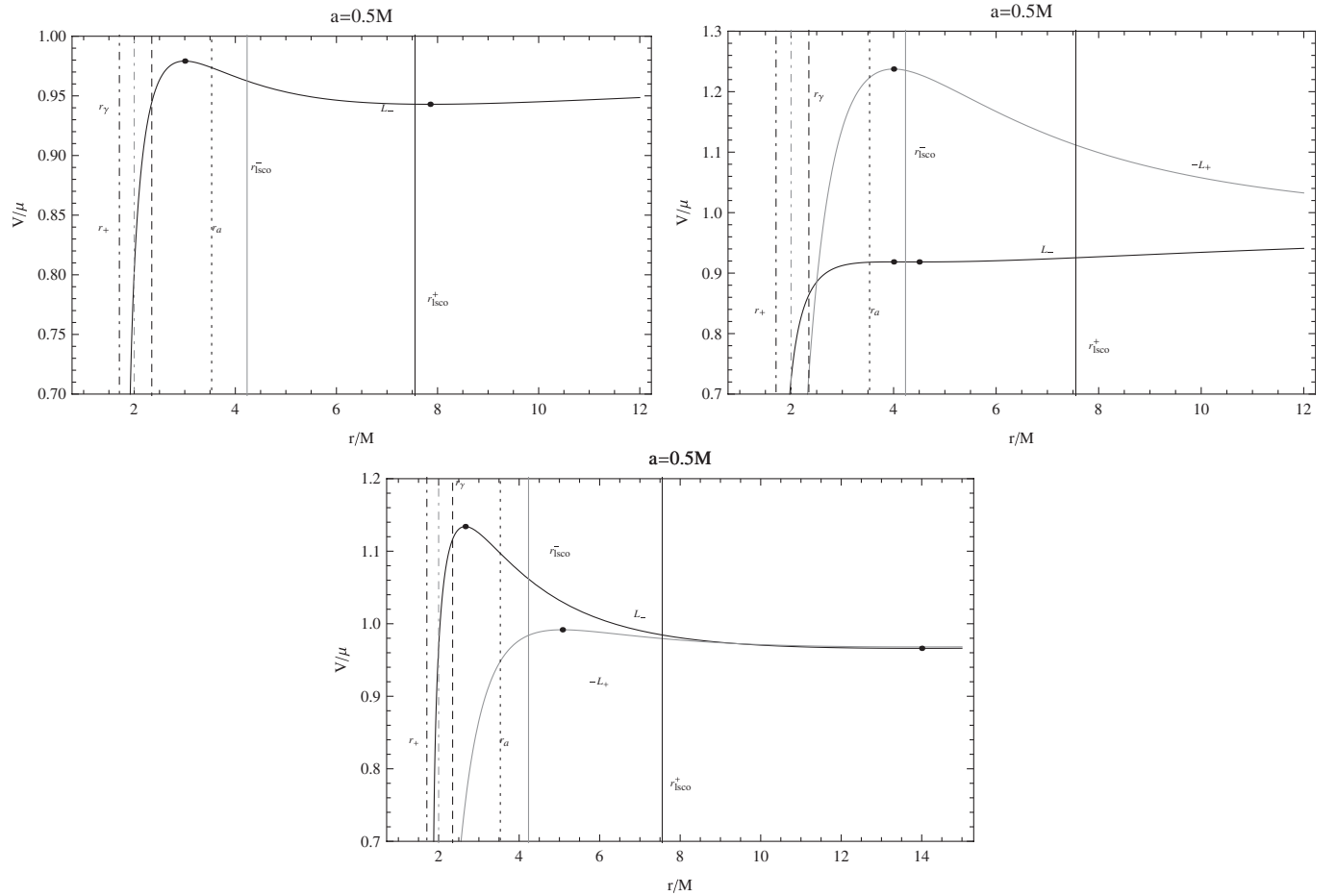
$$\partial^2 V / \partial^2 r = 0. \tag{27}$$

FIG. 8. The effective potential V/μ of a Kerr black hole with $a = 0.5M$ as a function of r/M. The radii $r_+ = 1.707\,11M$, $r_\gamma = 2.3473M$, $r_a = 3.532\,09M$, $r_{\text{lsco}}^- = 4.233M$, and $r_{\text{lsco}}^+ = 7.554\,58M$ are also plotted. The left upper plot shows the effective potential with orbital angular momentum $L = L_- = 3.298\,06M\mu$ for which we find a minimum (stable orbit) at $r = 7.852\,56M$ with energy $E_-/\mu = 0.942\,949$ and a maximum (unstable orbit) at $r = 3M$ with $E_-/\mu = 0.979\,181$. The right upper plot corresponds to an effective potential with orbital angular momentum $L = L_- = 2.908\,77\mu$ (solid black curve) and $L = -L_+ = -6.452\,35M\mu$ (solid gray curve). For $L = L_-$ there is a minimum (stable orbit) at $r = 4.499\,25M$ with $E_- = 0.918\,487\mu$ and a maximum (unstable orbit) at $r = 4M$ with $E_- = 0.918\,559\mu$. For $L = -L_+$ there is a maximum (unstable orbit) at $r = 4M$ with $E_+^{(-)} = 1.237\,44\mu$. The bottom plot is for an effective potential with orbital angular momentum $L = L_- = 4.096\,49\mu$ (solid black curve) and $L = -L_+ = -4.360\,42M\mu$ (solid gray curve). For $L = L_-$ there is a minimum (stable orbit) at $r = 14M$ with $E_- = 0.966\,09\mu$ and a maximum (unstable orbit) at $r = 2.659\,96M$ with $E_- = 1.134\mu$. For $L = -L_+$ there is a maximum (unstable orbit) at $r = 5.074\,11M$ with $E_+^{(-)} = 0.991\,686\mu$ and a minimum (stable orbit) at $r = 14M$ with $E_+^{(-)} = 0.968\,052\mu$. The dash-dotted gray line represents the outer boundary of the ergosphere $r_+^0 = 2M$.

The behavior of the effective potential (8) for a fixed value of a/M and different values of the particle angular momentum $L/(M\mu)$ is sketched in Fig. 4. The radii of the last stable circular orbits are written as [9,38]

$$r_{\text{lsco}}^{\mp} = M[3 + Z_2 \mp \sqrt{(3 - Z_1)(3 + Z_1 + 2Z_2)}], \quad (28)$$

where

$$Z_1 \equiv 1 + \left(1 - \frac{a^2}{M^2}\right)^{1/3}\left[\left(1 + \frac{a}{M}\right)^{1/3} + \left(1 - \frac{a}{M}\right)^{1/3}\right], \quad (29)$$

and

$$Z_2 \equiv \sqrt{3\frac{a^2}{M^2} + Z_1^2}. \quad (30)$$

In particular, for $a = 0$ we have that $r_{\text{lsco}}^{\mp} = 6M$, and when $a = M$ we obtain $r_{\text{lsco}}^{-} = M$ for corotating orbits and $r_{\text{lsco}}^{+} = 9M$ for counterrotating orbits (see also Fig. 5). In general, the radii r_{lsco}^{+} and r_{lsco}^{-} correspond to the last stable circular orbit of a test particle with angular momentum L_+ and L_-, respectively.

In Fig. 6 the energy $E_{\text{lsco}}^{\pm}/\mu = E(r_{\text{lsco}}^{\pm})/\mu$ and the angular momentum $L_{\text{lsco}}^{\pm}/\mu = L(r_{\text{lsco}}^{\pm})/\mu$ of the last stable circular orbits are plotted as functions of the ratio a/M. One can see that

$$E_{\text{lsco}}^{+} \leq E_{\text{lsco}}^{-}, \quad \text{and} \quad E_{\text{lsco}}^{+} = E_{\text{lsco}}^{-} \quad \text{for } a = 0. \quad (31)$$

Moreover, as the ratio a/M increases, the energy E_{lsco}^{+} decreases and the energy E_{lsco}^{-} increases. Instead, the

corresponding angular momenta of the test particles decrease as the intrinsic angular momentum increases.

To classify the circular orbits in a Kerr black hole it is convenient to distinguish two different regions: The first one is $a \in [0, \tilde{a}[$, where $\tilde{a} \approx 0.638\,285M$ is the value at which r_a and r_{lsco}^{-} coincide, and the second one is $a \in]\tilde{a}, 1[$.

In the first region $a \in [0, \tilde{a}[$, where $r_a < r_{\text{lsco}}^{-}$, we see that there exist unstable circular orbits with $L = L_-$ in the interval $r_\gamma < r < r_a$. Moreover, in the interval $r_a < r < r_{\text{lsco}}^{-}$ there are unstable circular orbits with $L = L_-$ and $L = -L_+$. In $r_{\text{lsco}}^{-} < r < r_{\text{lsco}}^{+}$ there are stable circular orbits with $L = L_-$ and unstable circular orbits with $L = -L_+$. Finally, in the region $r > r_{\text{lsco}}^{+}$ there are stable circular orbits with $L = L_-$ as well as with $L = -L_+$.

Let us consider the second region $a \in]\tilde{a}, 1[$ where $r_a > r_{\text{lsco}}^{-}$. We see that in the interval $r_\gamma < r < r_{\text{lsco}}^{-}$ there are unstable circular orbits with $L = L_-$. Moreover, in $r_{\text{lsco}}^{-} < r < r_a$ there are stable orbits with $L = L_-$. In the region $r_a < r < r_{\text{lsco}}^{+}$ there are stable circular orbits with $L = L_-$ and unstable orbits with $L = -L_+$. Finally, for $r > r_{\text{lsco}}^{+}$ there are stable circular orbits with $L = L_-$ and $L = -L_+$. The classification of circular orbits in this case is summarized in Table I.

A detailed analysis of the behavior of the energy, angular momentum, and effective potential of test particles is presented in Figs. 7 and 8 for $a/M = 0.5 < \tilde{a}$, in Figs. 9 and 10 for $a/M = 0.7 > \tilde{a}$, and finally in Figs. 11 and 12 for the limiting case of an extreme black hole $a/M = 1$.

To present the main result of our analysis in a plausible manner it is convenient to introduce the idea of a
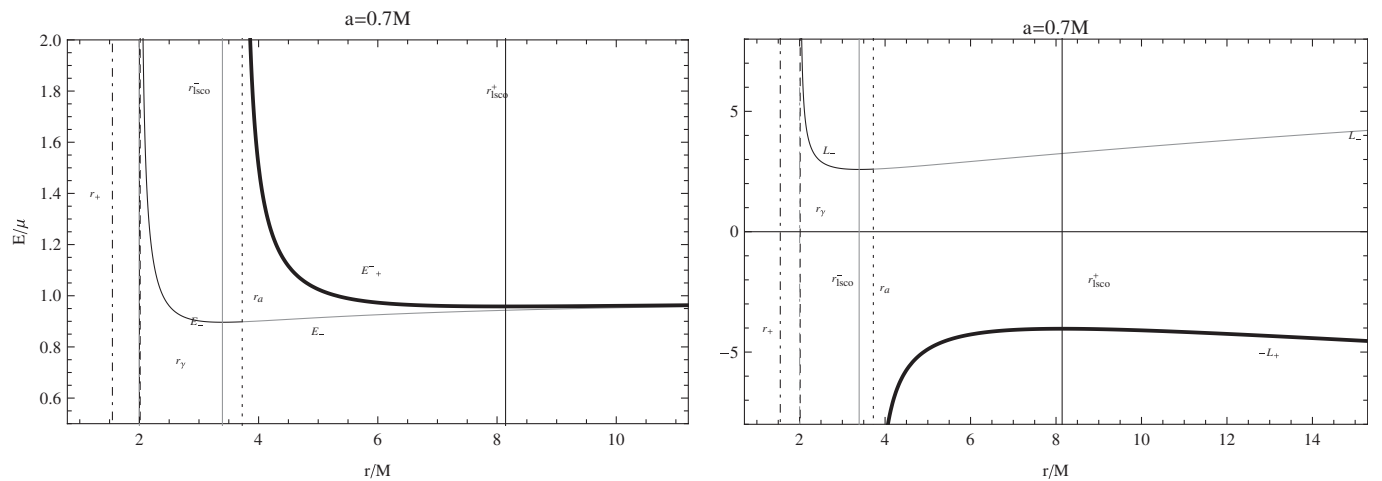

FIG. 9.   The energy E/μ (left plot) and the angular momentum $L/(\mu M)$ (right plot) of circular orbits in a Kerr black hole with $a = 0.7M$ as functions of r/M. The energy $E_+^- \equiv E(-L_+)$ and the angular momentum $-L_+$ are represented by thick solid black curves, and the energy $E_-^\pm \equiv E(L_-)$ and the angular momentum L_- by thin solid black curves. The radii $r_+ = 1.547\,72M$, $r_\gamma = 2.013\,33M$, $r_a = 3.725\,35M$, $r_{\text{lsco}}^{-} = 3.393\,13M$, and $r_{\text{lsco}}^{+} = 8.142\,97M$ are also plotted. The dash-dotted gray line represents the outer boundary of the ergosphere $r_+^0 = 2M$. In $r_\gamma < r < r_{\text{lsco}}^{-}$ there are unstable circular orbits with L_-; in $r_{\text{lsco}}^{-} < r < r_a$ there are stable orbits with L_-; in $r_a < r < r_{\text{lsco}}^{+}$ there are stable orbits with L_- and unstable with $-L_+$; finally, for $r > r_{\text{lsco}}^{+}$ there are stable circular orbits with L_- and $-L_+$. It is clear that $E(-L_+) > E(L_-)$.

hypothetical accretion disk formed by test particles on circular orbits around the central massive object. We consider this model only in the region $r > r_+^0$. The structure of such an accretion disk depends explicitly on the stability properties of the test particles. In fact, as mentioned above, the radii r_{lsco}^- and r_{lsco}^+ represent the last stable orbits for particles with angular momentum $L = L_-$ (corotating particles) and $L = -L_+$ (counterrotating particles), respectively. Then, in the disk contained within the radii $[r_{\text{lsco}}^-, r_{\text{lsco}}^+]$ only the corotating particles can move along

stable trajectories. If a counterrotating particle is located inside this disk (this is possible if the radius of the orbit is $r > r_a$), its orbit is unstable and it must decay into an orbit with radius $r > r_{\text{lsco}}^+$. Consequently, the outer disk with $r > r_{\text{lsco}}^+$ can be built of corotating and counterrotating particles which are both stable in this region. The size of the inner disk $[r_{\text{lsco}}^-, r_{\text{lsco}}^+]$ depends on the value of the intrinsic angular momentum of the black hole a; the maximum size is reached in the case of an extreme black hole ($a = M$) with $r_{\text{lsco}}^+ - r_{\text{lsco}}^- = 8M$ whereas for $a = 0$ the
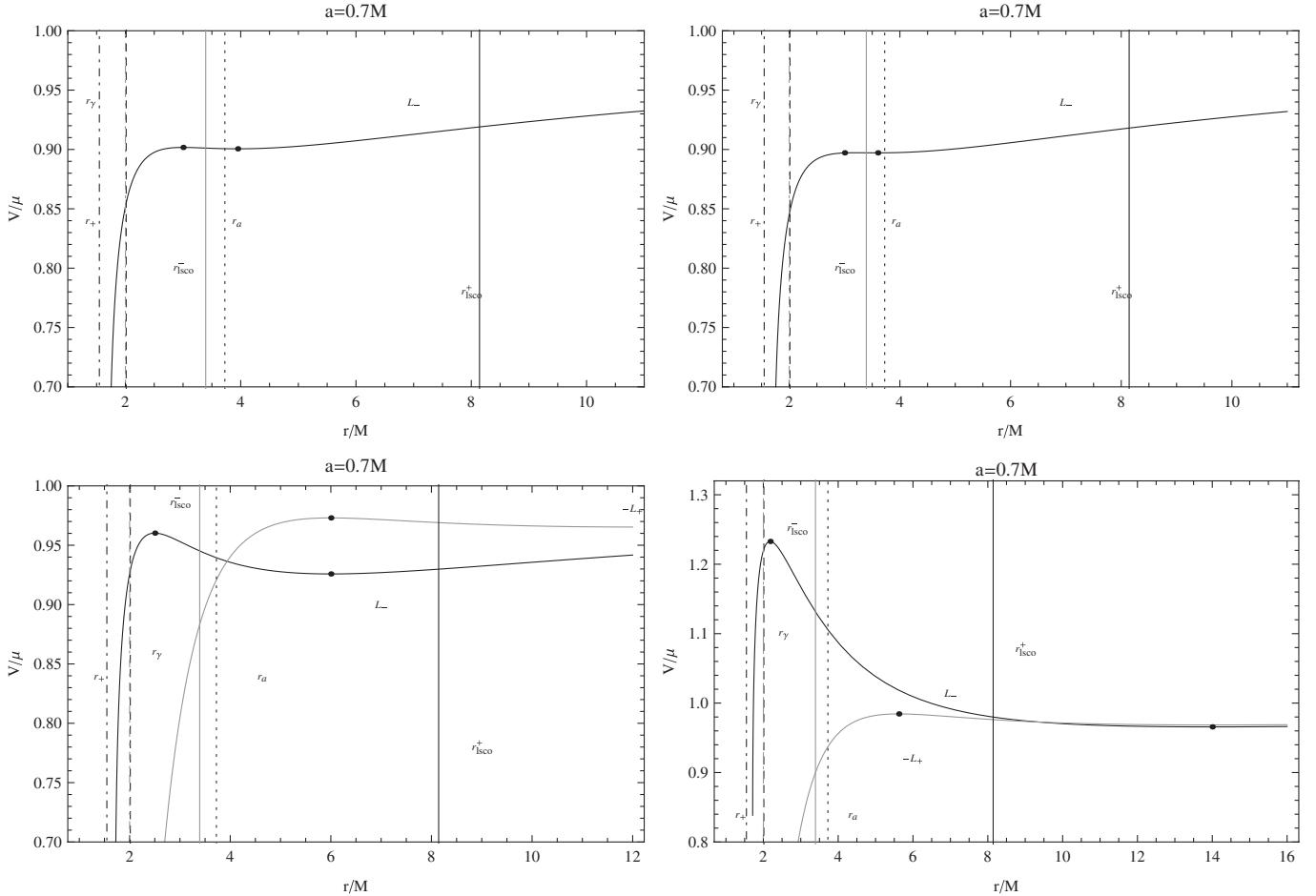

FIG. 10.   The effective potential V/μ of a Kerr black hole spacetime with $a = 0.7M$ as function of r/M. The radii $r_+ = 1.547\,72M$, $r_\gamma = 2.013\,33M$, $r_a = 3.725\,35M$, $r_{\text{lsco}}^- = 3.393\,13M$, and $r_{\text{lsco}}^+ = 8.142\,97M$ are plotted. The left upper plot represents the effective potential with orbital angular momentum $L = L_- = 2.619\,48M\mu$ for which we find a minimum (stable orbit) at $r = 3.9473M$ with $E_- = 0.900\,551\mu$, and a maximum (unstable orbit) at $r = 3M$ with $E_- = 0.901\,712\mu$. The right upper plot shows an effective potential with orbital angular momentum $L = L_- = 2.592\,16M\mu$ for which there exists a minimum (stable orbit) at $r = 3.6M$ with $E_- = 0.897\,167\mu$, and a maximum (unstable orbit) at $r = 3M$ with $E_- = 0.897\,167\mu$. The left bottom plot corresponds to effective potentials with orbital angular momenta $L = L_- = 2.915\,63\mu$ (solid black curve) and $L = -L_+ = -4.2694M\mu$ (solid gray curve). For $L = L_-$ there is a minimum (stable orbit) at $r = 6.M$ with $E_- = 0.925\,818\mu$, and a maximum (unstable orbit) at $r = 2.500\,52M$ with $E_- = 0.960\,213\mu$. For $L = -L_+$ there is a maximum (unstable orbit) at $r = 6M$ with $E_+^{(-)} = 0.973\,034\mu$. The right bottom plot is for effective potentials with orbital angular momenta $L = L_- = 4.050\,58\mu$ (solid black curve) and $L = -L_+ = -4.420\,36M\mu$ (solid gray curve). For $L = L_-$ there is a minimum (stable orbit) at $r = 14M$ with $E_- = 0.965\,775\mu$, and a maximum (unstable orbit) at $r = 2.1819M$ with $E_- = 1.232\,83\mu$. For $L = -L_+$ there is a maximum (unstable orbit) at $r = 5.6208M$ with $E_+^{(-)} = 0.984\,43\mu$, and a minimum (stable orbit) at $r = 14M$ with $E_+^{(-)} = 0.968\,527\mu$. The dash-dotted gray line represents the outer boundary of the ergosphere $r_+^0 = 2M$.
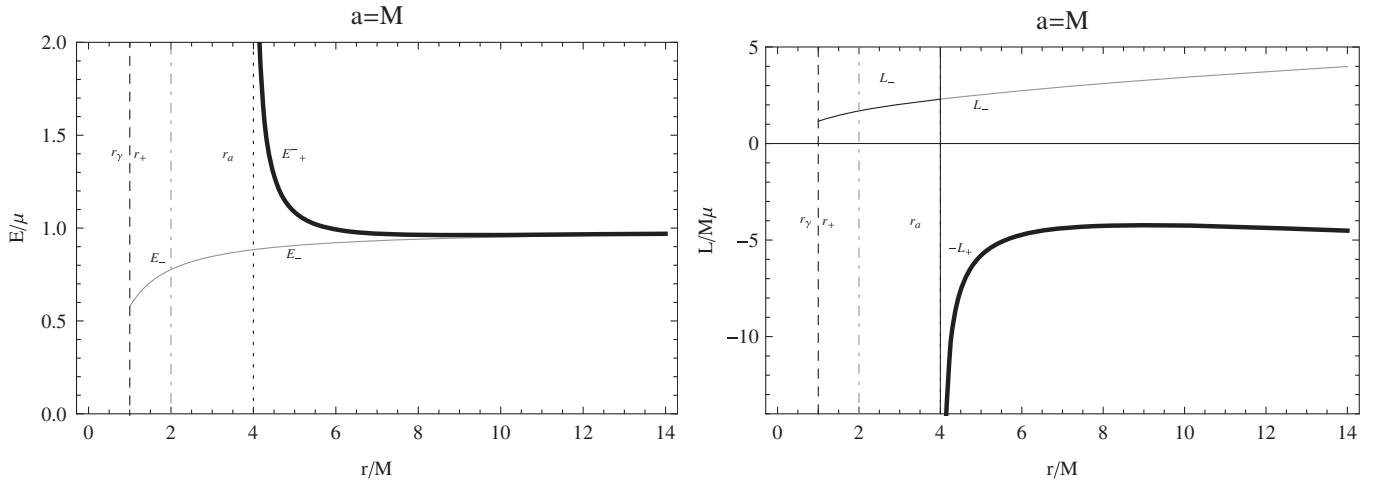
FIG. 11.   The energy E/μ (left plot) and the angular momentum $L/(\mu M)$ (right plot) of circular orbits in an extreme Kerr black hole ($a = M$) as functions of the radial coordinate r/M. The energy $E(-L_+)$ and the angular momentum $-L_+$ are represented by thick solid black curves, and the energy $E(L_-)$ and the angular momentum L_- by thin solid black curves. The radii $r_+ = r_\gamma = M$ (dashed curve) and $r_a = 4M$ (solid black curve) are also plotted. There exist circular orbits with $L = L_-$ in $r > r_\gamma$. The energy $E(L_-)$ is always positive and decreases as r approaches r_γ. Circular orbits with $L = -L_+$ exist also in $r > r_+$. The energy $E(-L_+)$ is always positive and increases as r approaches r_a. It is evident that $E(-L_+) > E(L_-)$.
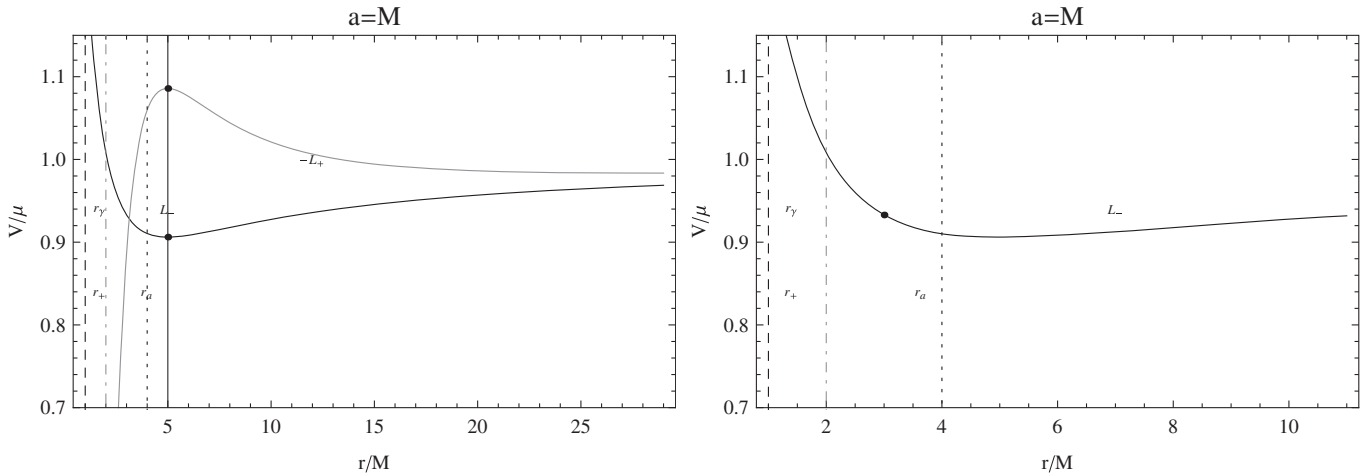
FIG. 12.   The effective potential V/μ of an extreme Kerr black hole for a test particle with a fixed orbital angular momentum as function of r/M. The radii $r_+ = r_\gamma = M$ (dashed curve) and $r_a = 4M$ (solid black curve) are plotted. The dash-dotted gray line represents the outer boundary of the ergosphere $r_+^0 = 2M$. The left plot shows the effective potentials with orbital angular momenta $L = L_-$ (solid black curve) and $L = -L_+$ (solid gray curve). For $L = L_-$ there is a minimum (stable orbit) at $r = 5M$ with $L_- = 2.530\,75M\mu$ and $E_- = 0.906154\mu$. For $L = -L_+$ there is a maximum (unstable orbit) at $r = 5M$ with $-L_+ = -5.796\,14M\mu$ and $E_+^- = 1.085\,76\mu$. There exist circular orbits with $L = L_-$ in the region $r > r_\gamma$, and orbits with $L = -L_+$ in the region $r > r_+$. The dash-dotted gray line represents the outer boundary of the ergosphere $r_+^0 = 2M$.

radii coincide $r_{\text{lsco}}^+ = r_{\text{lsco}}^-$ and the disk disappears (cf. Fig. 5).

IV. NAKED SINGULARITIES

In the naked singularity case ($a > M$), it is $g_{tt} > 0$ for $0 < r < r_-^0$ and $r > r_+^0$ when $0 \le \cos^2\theta < 1/a^2$, for $r > 0$ with $r \ne r_-^0$ when $\cos^2\theta = 1/a^2$, and finally for $r > 0$ when $1/a^2 < \cos^2\theta \le 1$. Moreover, $g_{tt} = 0$ at $r = 2M$ if $\theta = \pi/2$, at $r = r_\pm^0$ for $0 < \cos^2\theta < 1/a^2$, and at $r = r_-^0$ for $\cos^2\theta = 1/a^2$. As in the black hole case, in the region (r_-^0, r_+^0) the Killing vector $\xi_t^a = (1, 0, 0, 0)$ becomes space-like. On the equatorial plane, $\theta = \pi/2$, it is $r_+^0 = 2M$ and $r_-^0 = 0$. In this case, the timelike Killing vector becomes spacelike in the region $0 < r < r_+^0$, for all $a > M$.

According to the results presented in Sec. II, to explore the motion of test particles along circular orbits we must solve the following equations
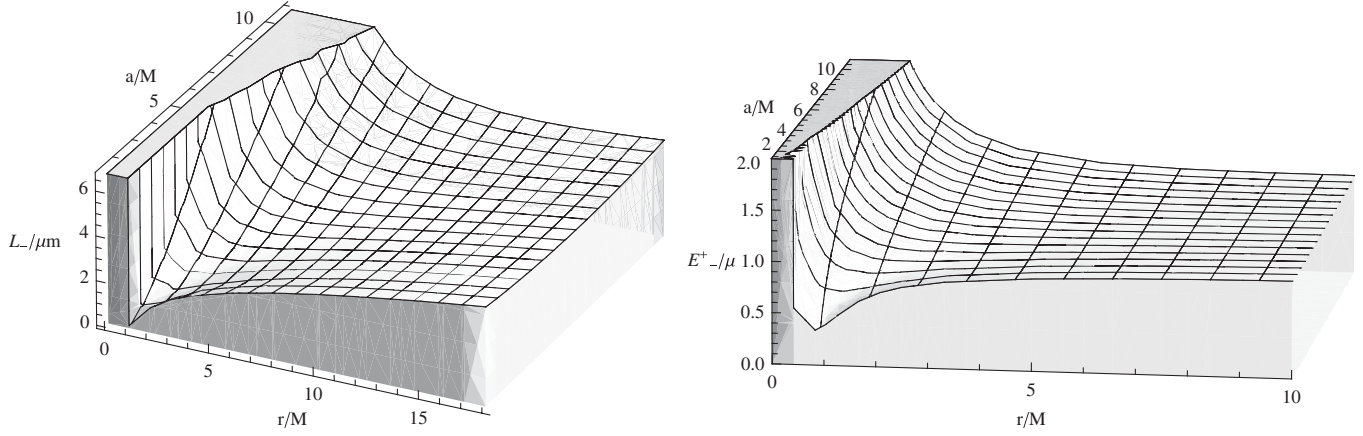
FIG. 13.   Angular momentum and energy of test particles in a Kerr naked singularity with $a \geq (3\sqrt{3}/4)M$. The angular momentum $L = L_-$ (left plot) and the energy $E_-^{(+)} \equiv E(L_-)$ (right plot) of circular orbits are plotted as functions of $r > 0$ and $a \geq (3\sqrt{3}/4)M$. The particle's energy is always positive. It is possible to note a region of minima for the energy corresponding to the minima of L_-.
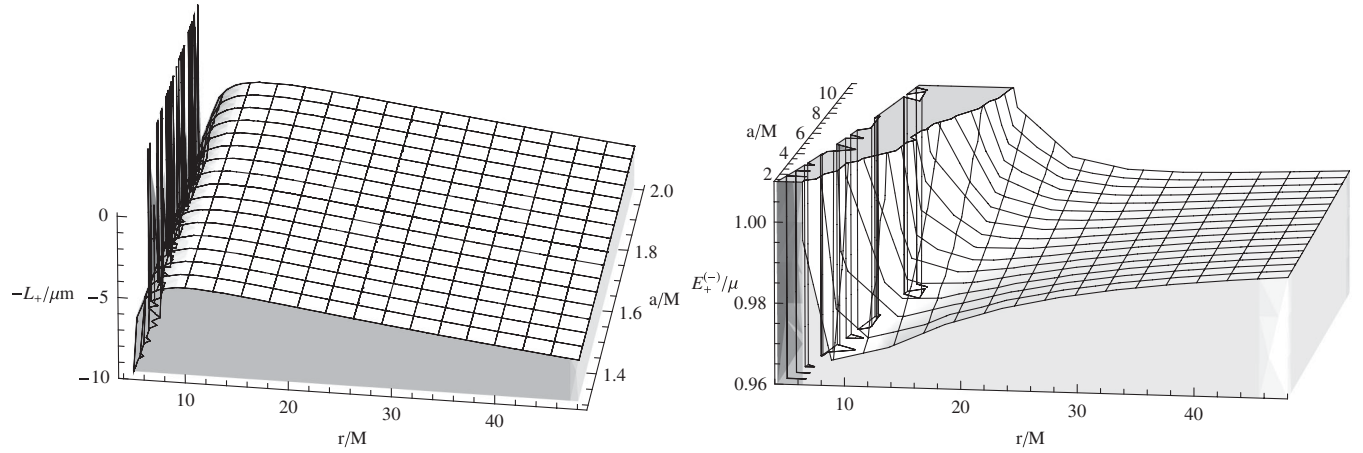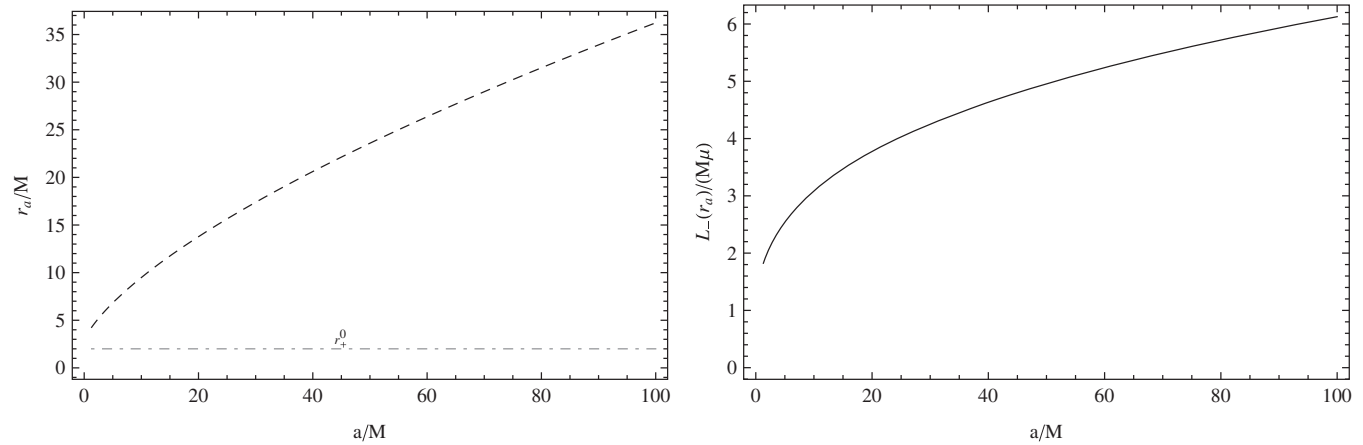

FIG. 14.   Angular momentum and energy of test particles in a Kerr naked singularity with $a \geq (3\sqrt{3}/4)M$. The angular momentum $L = -L_+$ (left plot) and the energy $E_+^{(-)} \equiv E(-L_+)$ (right plot) of circular orbits are plotted as functions of $r > r_a$ and $a \geq (3\sqrt{3}/4)M$. The particle's energy is always positive. It is possible to note a region of minima for the energy corresponding to the minima of $-L_+$.

FIG. 15.   The graphic shows the radius r_a/M (left plot) as a function of the intrinsic angular momentum parameter a/M in the interval $(3\sqrt{3}/4, 100)$, and the particle orbital angular momentum $L(r_a)/(\mu M)$ (right plot) as a function of a/M. The dash-dotted gray line represents the outer boundary of the ergosphere $r_+^0 = 2M$.
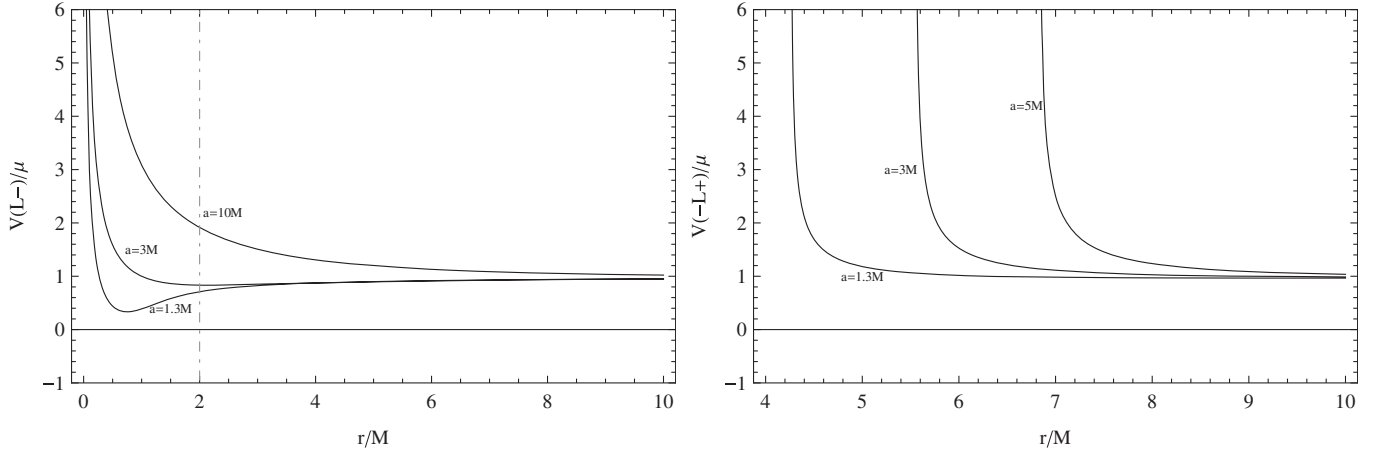
FIG. 16.   The energy of circular orbits in a Kerr naked singularity with source angular momentum $a \geq (3\sqrt{3}/4)M$ is plotted in terms of the radial coordinate r/M for selected values of a/M. The left plot corresponds to particles with $L = L_-$, and the right plot is particles with $L = -L_+$. The energy is always positive and diverges as the limiting radius is approached. The dash-dotted gray line represents the outer boundary of the ergosphere $r_+^0 = 2M$.

$$\dot{r} = 0, \qquad V = E/\mu, \qquad \partial V/\partial r = 0 \qquad (32)$$

for the effective potential (8) with $a > M$, taking into account that in this case no horizons exist. It turns out that it is convenient to study separately the range $a \geq 3\sqrt{3}/4M$ (see Sec. IV A) and the range $M < a < 3\sqrt{3}/4M$ (see Sec. IV B) for the values of the intrinsic angular momentum of the naked singularity.

A. The case $a \geq (3\sqrt{3}/4)M$

In this case we find that for all $r > 0$ there exist circular orbits with angular momentum $L = L_-$ and energy $E_-^{(+)} = E(L_-)$. In Fig. 13 we illustrate the behavior of the energy and angular momentum of test particles for this case.

An analysis of the effective potential shows that a second class of circular orbits with $L = -L_+$ and energy $E_+^{(-)} = E(-L_+)$ can be found in the region $r > r_a$ where

$$\frac{r_a}{M} \equiv 2 + \frac{1 + (2\frac{a^2}{M^2} - 1 + 2\sqrt{\frac{a^4}{M^4} - \frac{a^2}{M^2}})^{2/3}}{(2\frac{a^2}{M^2} - 1 + 2\sqrt{\frac{a^4}{M^4} - \frac{a^2}{M^2}})^{1/3}}. \qquad (33)$$

The expression for the energy and angular momentum of the test particles in this region is depicted in Fig. 14.

The special radius r_a and the angular momentum for this radius $L(r_a)/(\mu M)$ increase as the intrinsic angular momentum of the naked singularity increases, as shown in Fig. 15. Notice that we are using the same notation r_a for the radius (18) of a black hole and the radius (33) of
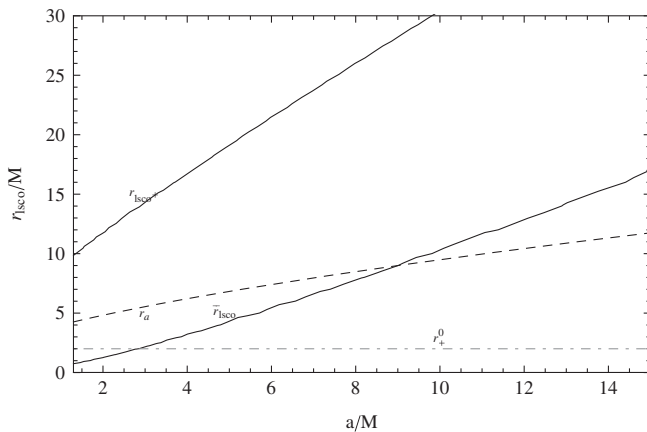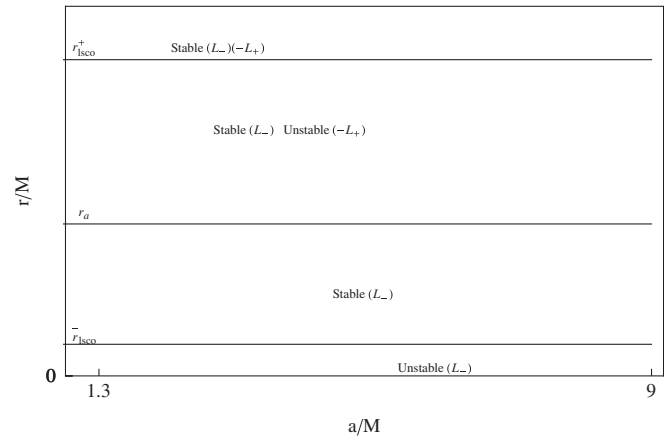

FIG. 17.   Radius of the last stable circular orbits for test particles in a Kerr naked singularity with $a \geq \frac{3\sqrt{3}}{4}M$. The dash-dotted gray line represents the outer boundary of the ergosphere $r_+^0 = 2M$. The radius $\bar{r}_{\mathrm{lsco}}$ (r_{lsco}^+) is the limiting minimum radius of stability for particles with $L = L_-$ ($L = -L_+$).

FIG. 18.   Orbits' stability in a Kerr naked singularity with $\frac{3\sqrt{3}}{4}M \leq a \lesssim 9$. The different radii of the last stable circular orbits r_{lsco} are plotted in terms of the intrinsic angular momentum a/M.

a naked singularity. Although these radii are different in their definitions, we use the same notation because in the limiting case $a = M$ they both have the same limiting value $r_a = 4M$. This will turn out later on to be convenient when we compare the results of black holes with those of naked singularities.

The energies $E(L_-)$ and $E(-L_+)$ for the two classes of test particles allowed in this are compared in Fig. 16. For particles with angular momentum $L = L_-$ we see that the energy diverges as the limiting value $r \to 0$ is approached. Similarly, for particles with $L = -L_+$ the energy diverges as the radius approaches the limiting value $r \to r_a$, indicating that the orbit located at $r = r_a$ is lightlike.

We now study the stability of the test particles in this specific case. An analysis of the turning points of the potential (8) indicates that the radius of the last stable circular orbit for particles with $L = L_-$ (located in the region $r > 0$) is given by
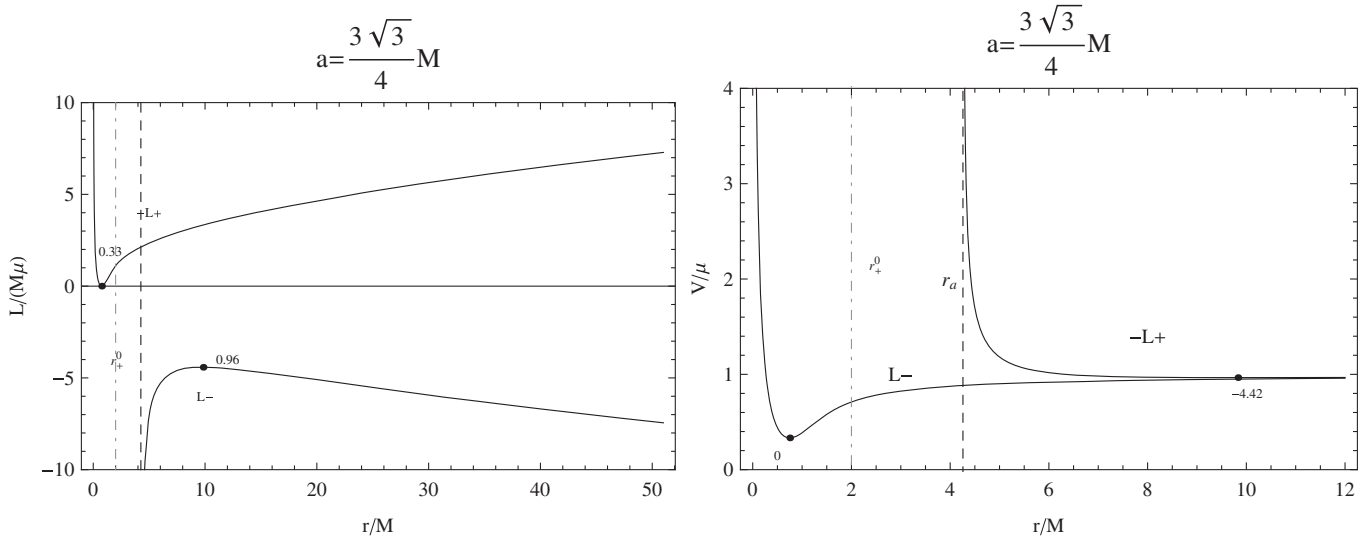

FIG. 19.   The angular momentum and the energy of test particles in the field of a Kerr naked singularity with $a = 3\sqrt{3}/4M \approx 1.30M$ are plotted as functions of the radial coordinate r/M. The dots represent the last stable circular orbits; numbers close to the points denote the energy V/μ of the last stable circular orbit. For $r > r_a \approx 4.2592M$ there exist circular orbits with angular momentum $L = -L_+$, and for all $r > 0$ with $L = L_-$ (see text). For $r = 0.75M$ the particle has $L = 0$ and energy $E \approx 0.333M$. The dash-dotted gray line represents the outer boundary of the ergosphere $r_+^0 = 2M$.
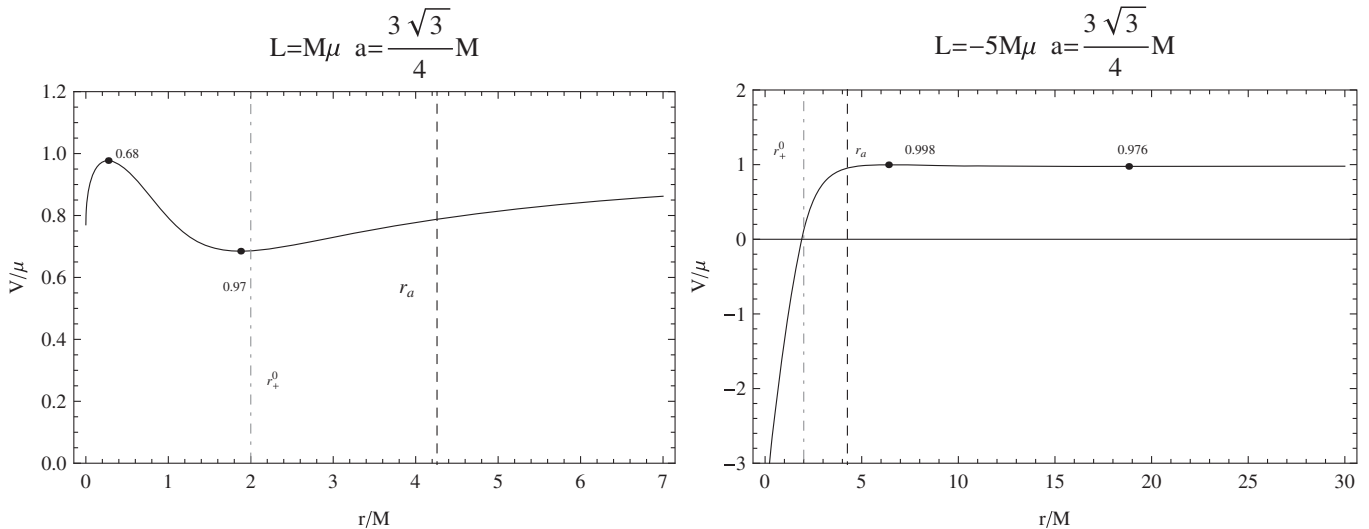

FIG. 20.   The effective potential of a naked singularity with $a = \frac{3\sqrt{3}}{4}M$ for fixed values of the particle angular momentum $L/(M\mu)$. The dash-dotted gray line represents the outer boundary of the ergosphere $r_+^0 = 2M$. The radius r_a is also plotted (see text). The dots denote the critical points of the potential. Numbers close to the dots denote the energy V/μ of the maxima and minima of the effective potential.
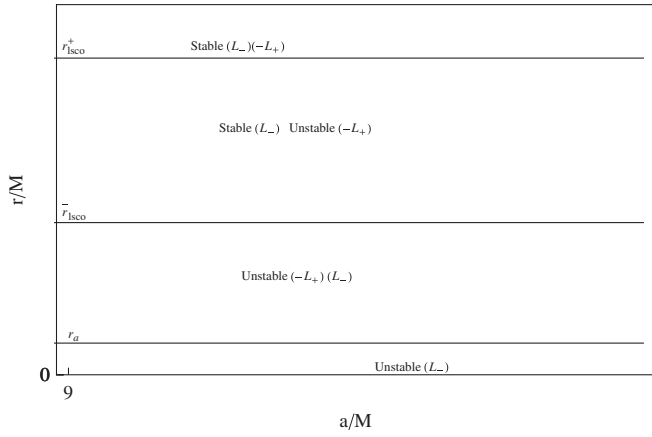
FIG. 21. Orbits' stability in a Kerr naked singularity with $a \gtrsim 9M$. The radii $r_{\rm lsco}$ of the last stable circular orbits are plotted as functions of the intrinsic angular momentum a/M. The radius $r = r_a$ is also plotted.

$$\bar{r}_{\rm lsco} \equiv M(3 - Z_2 + \sqrt{(3 - Z_1)(3 + Z_1 - 2Z_2)}), \quad (34)$$

where Z_1 and Z_2 were defined in Eqs. (29) and (30), respectively. Moreover, for particles with $L = -L_+$ located at $r > r_a$ there exists a minimum radius $r = r_{\rm lsco}^+$ for the last stable circular orbit. The expression for $r_{\rm lsco}^+$ is given in Eq. (28). The behavior of this limiting radii in terms of the intrinsic angular momentum of the naked singularity is depicted in Fig. 17. It follows that both radii increase as the value of a/M increases.

It turns out that it is necessary to distinguish two different regions, namely, $a/M \in [3\sqrt{3}/4, 9]$ and $a/M \in\,]9, +\infty[$.

1. The region $a/M \in [3\sqrt{3}/4, 9]$

In the first region $a/M \in [3\sqrt{3}/4, 9]$ which is characterized by

$$\bar{r}_{\rm lsco} < r_a < r_{\rm lsco}^+, \quad \text{and} \quad \bar{r}_{\rm lsco} = r_a \quad \text{for } a \approx 9M, \quad (35)$$

there exist unstable circular orbits with $L = L_-$ in the interval $0 < r < \bar{r}_{\rm lsco}$, and stable orbits with $L = L_-$ in the interval $\bar{r}_{\rm lsco} < r < r_a$. Moreover, in the region $r_a < r < r_{\rm lsco}^+$ there are stable orbits with angular momentum $L = L_-$, and unstable orbits with angular momentum $L = -L_+$. Finally, for $r > r_{\rm lsco}^+$ there are stable orbits with $L = L_-$ and $L = -L_+$. In Fig. 18 we present a summary of this case.

As a concrete example for this case we consider now the motion of test particles around a naked singularity with $a = \frac{3\sqrt{3}}{4}M$. In this case, circular orbits with orbital angular momentum $L = L_-$ exist in the range $r > 0$, and with $L = -L_+$ in the range $r > r_a \approx 4.259M$. The energy and angular momentum of these circular orbits are plotted in Fig. 19.

In Fig. 20 the effective potential is plotted for different values of the orbital angular momentum. In particular, an "orbit" with zero angular momentum ($L = 0$) and energy $E \approx 0.333M$ exists for $r = 0.75M$ (see also Sec. IV C).

From the analysis of the effective potential it follows that the turning points are located at $r_{\rm lsco}^+ \approx 9.828M$ where $L_{\rm lsco}^+ \approx -4.421\mu M$ and $V_{\rm lsco}^+ \approx 0.96\mu$. Moreover, in the interval $0 < r < r_{\rm lsco}^-$ the orbits with angular momentum $L = L_-$ are unstable; in the interval $r_{\rm lsco}^- < r < r_a$ the orbits with $L = L_-$ are stable; and for $r_a < r < r_{\rm lsco}^+$ we see that the orbits with $L = L_-$ are stable and those with $L = -L_+$ are unstable. Finally, in the range $r > r_{\rm lsco}^+$, the orbits with $L = -L_+$ and $L = L_-$ are both stable.
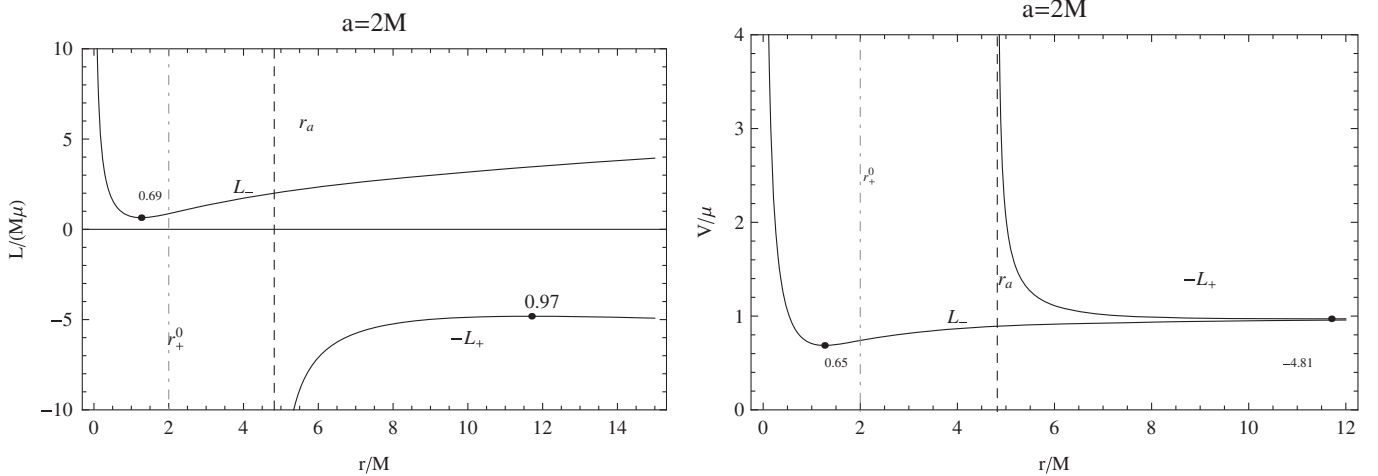

FIG. 22. The angular momentum and the energy of circular orbits in a Kerr naked singularity with $a = 2M$, as functions of the radial distance r/M. The dash-dotted gray line represents the outer boundary of the ergosphere $r_+^0 = 2M$. The dots denote the position of the last stable circular orbits, and the numbers close to the dots indicate the value of the corresponding energy V/μ or angular momentum $L/(M\mu)$. In the range $r > r_a \approx 4.822M$ there exist circular orbits with $L = -L_+$, and in $r > 0$ with $L = L_-$ (see text).

2. The region $\frac{a}{M} \in]9, +\infty[$

In the second region $(a \gtrsim 9M)$ which is characterized by

$$r_a < \bar{r}_{lsco} < r^+_{lsco}, \qquad (36)$$

there are unstable orbits with angular momentum $L = L_-$ in the interval $0 < r < r_a$ and with $L = L_-$ and $L = -L_+$ in the interval $r_a < r < \bar{r}_{lsco}$. Moreover, for $\bar{r}_{lsco} < r < r^+_{lsco}$ there are stable orbits with $L = L_-$ and unstable ones with $L = -L_+$. Finally, for $r > r^+_{lsco}$ there are stable orbits with both $L = L_-$ and $L = -L_+$. In Fig. 21 a schematic summary of this case is presented.

As a concrete example of this case we now analyze the circular motion of test particles around a naked singularity with $a = 2M$. In this case, circular orbits with angular momentum $L = L_-$ exist in the entire range $r > 0$, and with $L = -L_+$ in the range $r > r_a \approx 4.822M$. The energy and the angular momentum of the circular orbits are plotted in Fig. 22.

In Fig. 23, the effective potential of circular orbits is plotted for selected values of the orbital angular momentum in terms of the radial distance. The turning points of the effective potential are $r^+_{lsco} \approx 11.702M$ for which $L^+_{lsco} \approx -4.814\mu M$ and $V^+_{lsco} \approx 0.971\mu$, and $r^-_{lsco} \approx 1.263M$ with $L^-_{lsco} \approx 0.645\mu M$ and $V^-_{lsco} \approx 0.687\mu$.
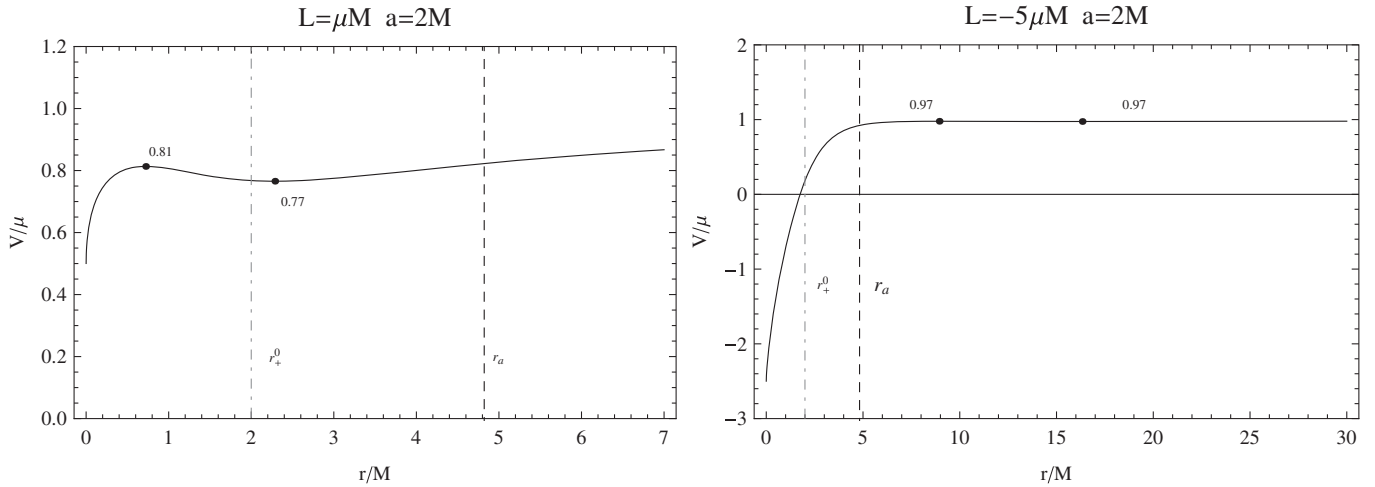

FIG. 23.   The effective potential of a naked singularity with $a = 2M$ for fixed values of the particle angular momentum $L/(M\mu)$. The radius r_a is also plotted (see text). The dash-dotted gray line represents the outer boundary of the ergosphere $r^0_+ = 2M$. The dots represent the critical points of the potential. Numbers close to the dots indicate the energy V/μ of the maxima and minima of the effective potential.
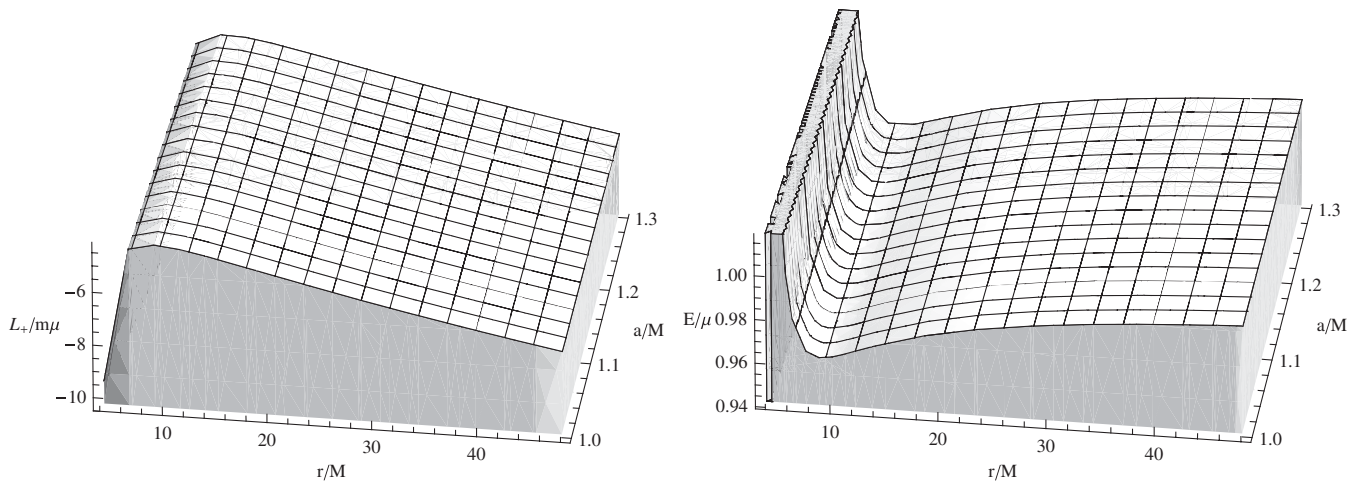

FIG. 24.   Circular motion around a naked singularity with $M < a < (3\sqrt{3}/4)M$. The angular momentum $L = -L_+$ (left plot) and the energy $E^{(-)}_+ \equiv E(-L_+)$ (right plot) for circular orbits are plotted as functions of a in the range $1 < a/M < 3\sqrt{3}/4$ and r in the range $r > r_a$. The particle energy is always positive with a region of minima corresponding to the minima of $-L_+$.

The distribution of circular orbits is as follows: In the interval $0 < r < \bar{r}_{\text{lsco}}$ there exist unstable orbits with $L = L_-$ which become stable for $\bar{r}_{\text{lsco}} < r < r_a$; in the interval $r_a < r < r_{\text{lsco}}^+$ the orbits with $L = L_-$ are stable while those with $L = -L_+$ are unstable. In the outer region $r > r_{\text{lsco}}^+$ orbits with $L = -L_+$ and $L = L_-$ are both stable. To illustrate the results of the analysis of this case, we consider in the region $r > r_+^0$ the model of an accretion disk made of stable particles moving on circular orbits around the central naked singularity. We find an accretion disk composed of an interior disk contained within the radii $[\bar{r}_{\text{lsco}}, r_{\text{lsco}}^+]$ in which stable

particles with angular momentum $L = L_-$ corotate with the central singularity. A second disk is located at $r > r_{\text{lsco}}^+$ and contains corotating particles with angular momentum $L = L_-$ and counterrotating particles with $L = -L_+$. We see that the structure of this accretion disk is similar to that found in Sec. III for black holes. The only difference is that in the case of a naked singularity the interior disk situated within the radii $[\bar{r}_{\text{lsco}}, r_{\text{lsco}}^+]$ has a minimum size of $r_{\text{lsco}}^+ - \bar{r}_{\text{lsco}} > 8M$, whereas in the case of a black hole the size of the inner disk is always less than $8M$ and disappears as $a \to 0$.
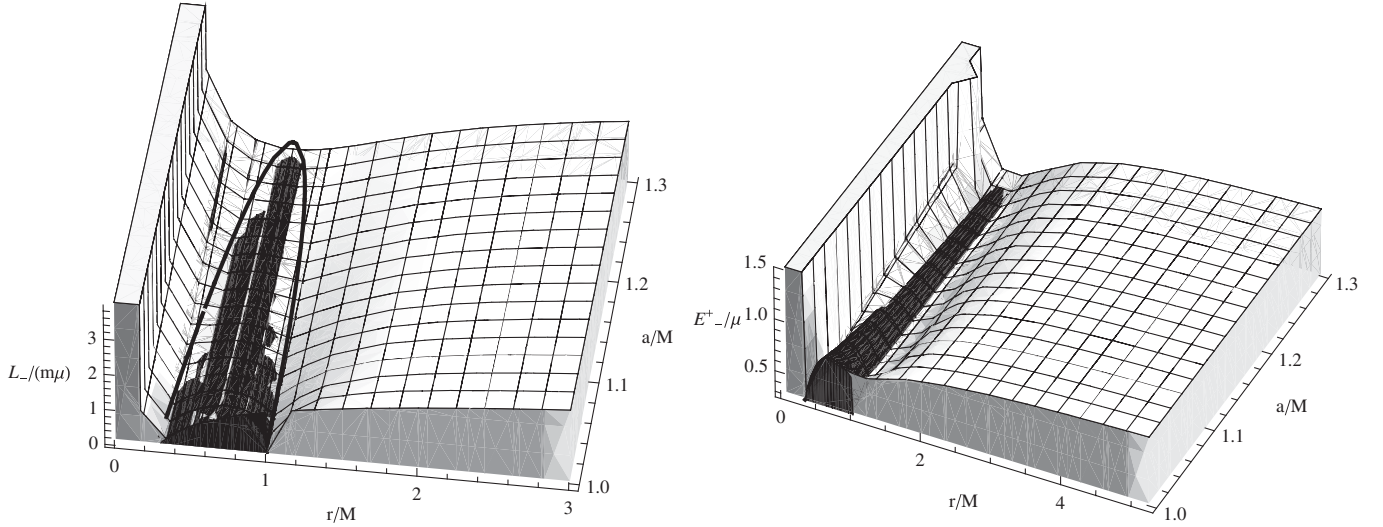

FIG. 25. Circular motion around a naked singularity with $M < a < (3\sqrt{3}/4)M$. The angular momentum $L = L_-$ (left plot) and the energy $E_- \equiv E(L_-)$ (right plot) of circular orbits are plotted as functions of a in the range $1 < a/M < 3\sqrt{3}/4$ and r in the intervals $r > \hat{r}_+$ and $0 < r < \hat{r}_-$. The region $\hat{r}_- < r < \hat{r}_+$ is represented as a dark region. As r/M approaches the singularity, the particle energy and angular momentum diverge. As r/M approaches $\hat{r}_-$ from the left and $\hat{r}_+$ from the right, the particle energy and angular momentum decrease.
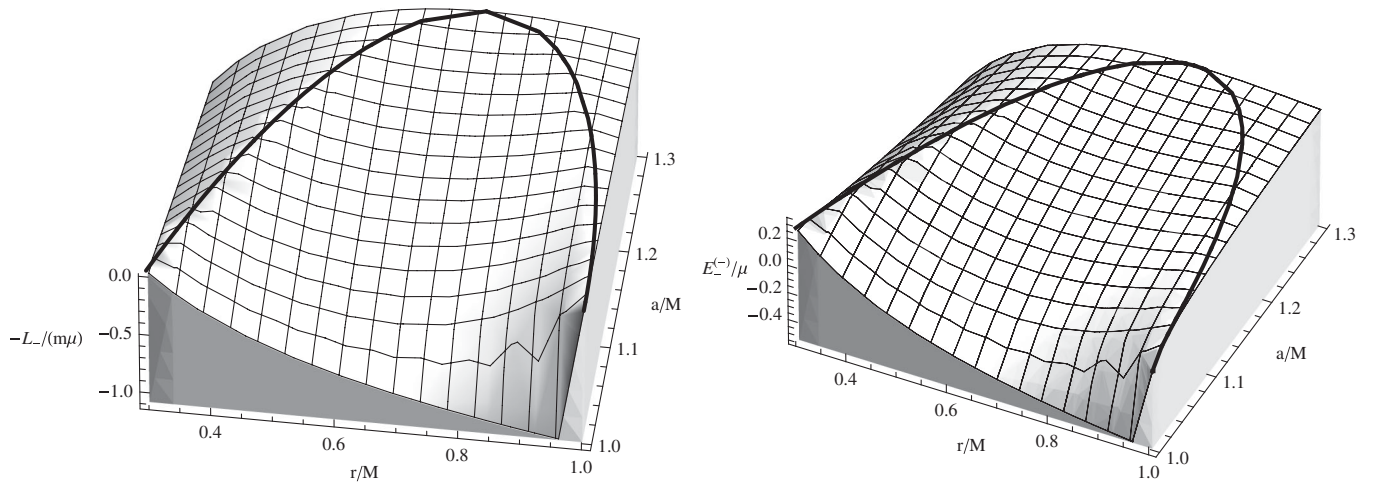

FIG. 26. Circular motion around a naked singularity with $M < a < (3\sqrt{3}/4)M$. The angular momentum $L = -L_-$ (left plot) and the energy $E^- \equiv E(-L_-)$ (right plot) of circular orbits are plotted as functions of a in the range $1 < a/M < 3\sqrt{3}/4$ and of r in the interval $\hat{r}_- < r < \hat{r}_+$. The solid black curves represent the radii $\hat{r}_-$ and $\hat{r}_+$. The presence of negative values for the particle energy is evident.

B. The case $M < a < (3\sqrt{3}/4)M$

For this range of values of the intrinsic angular momentum of the naked singularity we find that there are circular orbits with angular momentum $L = -L_+$ and energy $E(-L_+)$ only in the region $r > r_a$. In Fig. 24 we present the parameters for the circular orbits.

From the expression for the effective potential and the conditions for circular motion it follows that in this case two additional regions arise. Indeed, in the intervals $0 < r < \hat{r}_-$ and $r \geq \hat{r}_+$ there exist circular orbits with angular momentum $L = L_-$ and energy $E(L_-)$ (see Fig. 25). Moreover, in the interval $\hat{r}_- < r < \hat{r}_+$ we observe circular orbits with angular momentum $L = -L_-$ and energy $E(-L_-)$ (see Fig. 26), where

$$\hat{r}_\pm \equiv \frac{1}{\sqrt{6}}\left[\Sigma \pm \sqrt{\frac{6\sqrt{6}a^2 M}{\Sigma} - \Sigma^2 - 6a^2}\right], \quad (37)$$

with

$$\Sigma = \sqrt{\frac{4a^4}{\sigma^{1/3}} + \sigma^{1/3} - 2a^2}, \quad (38)$$

and

$$\sigma = (27M^2 a^4 - 8a^6 + 3M\sqrt{81M^2 a^8 - 48a^{10}}). \quad (39)$$

The behavior of these special radii is illustrated in Fig. 27.

Notice that the energy of circular orbits $E(-L_+)$ in the interval $0 < r < \hat{r}_-$ and in $r \geq \hat{r}_+$ (see Fig. 28), and the energy $E(L_-)$ in the interval $r > r_a$, are always positive (see Fig. 29). On the contrary, the energy $E(-L_-)$ of circular orbits within the region $\hat{r}_- < r < \hat{r}_+$ can be negative. In particular, we see that $E(-L_-) = 0$ for $a = \bar{a}$, where
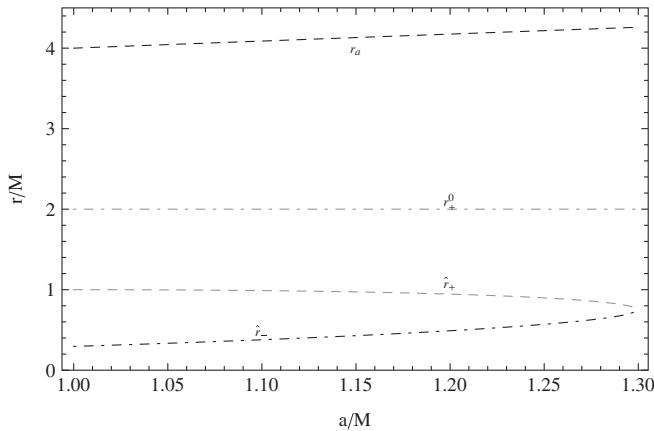
$$\bar{a} \equiv -(r - 2M)\sqrt{\frac{r}{M}}, \quad (40)$$

or for the orbital radii $r = \bar{r}_1$ and $r = \bar{r}_2$, where

$$\frac{\bar{r}_1}{M} \equiv \frac{8}{3}\sin\left(\frac{1}{6}\arccos\left[1 - \frac{27a^2}{16M^2}\right]\right)^2, \quad (41)$$

and

$$\frac{\bar{r}_2}{M} \equiv \frac{4}{3}\left(1 + \sin\left[\frac{1}{3}\arcsin\left[1 - \frac{27a^2}{16M^2}\right]\right]\right), \quad (42)$$

which are the solutions of the equation $a = \bar{a}$.

We can see that $E(-L_-) < 0$ for $M < a < \sqrt{32/27}M$ in the interval $\bar{r}_1 < r < \bar{r}_2$. Otherwise, for $a > \sqrt{32/27}M$, the energy $E(-L_-)$ is always strictly positive. This behavior is illustrated in Fig. 30.

The stability of circular orbits is determined by the turning points of the effective potential. For this case we find numerically two turning points r^+_{lsco} and $\tilde{r}^-_{\mathrm{lsco}}$ with $\hat{r}_- < \tilde{r}^-_{\mathrm{lsco}} < \hat{r}_+$ and $r^+_{\mathrm{lsco}} > r_a$ (see Fig. 31), where

$$\tilde{r}^-_{\mathrm{lsco}} \equiv 3 - Z_2 - \sqrt{(3 - Z_1)(3 + Z_1 - 2Z_2)}. \quad (43)$$

The radii r^+_{lsco} and $\tilde{r}^-_{\mathrm{lsco}}$ correspond to the last stable circular orbits with angular $L = -L_+$ and $L = -L_-$, respectively. Then, the distribution of circular orbits in the different regions is as follows:

(i) In the region $0 < r < \hat{r}_-$, the orbits with $L = L_-$ are unstable.

(ii) In the region $\hat{r}_- < r < \tilde{r}^-_{\mathrm{lsco}}$, the orbits with $L = -L_-$ are unstable.

(iii) In the region $\tilde{r}^-_{\mathrm{lsco}} < r < \hat{r}_+$, the orbits with $L = -L_-$ are stable.

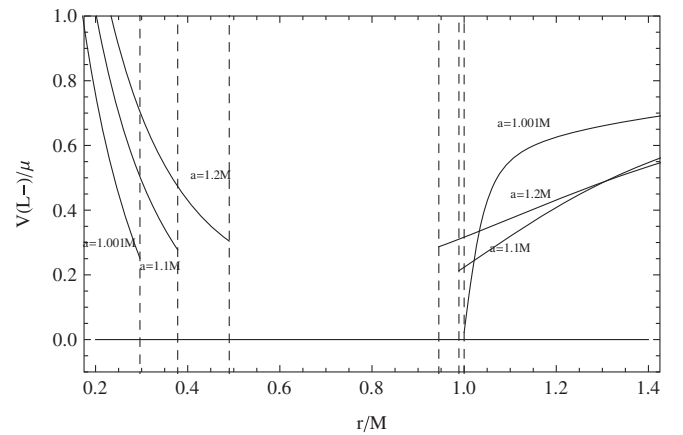(iv) In the region $\hat{r}_+ < r < r_a$, the orbits with $L = L_-$ are stable.

FIG. 27. The radii r_a and $\hat{r}_\pm$ are plotted as functions of a/M. Circular orbits with angular momentum $L = -L_+$ exist for $r > r_a$, with $L = L_-$ in $0 < r < \hat{r}_-$ and $r \geq \hat{r}_+$, and with $L = -L_-$ in $\hat{r}_- < r < \hat{r}_+$ (see text). The dash-dotted gray line represents the outer boundary of the ergosphere $r^0_+ = 2M$.

FIG. 28. The energy $E(L_-)$ of test particles is plotted for selected values of a in the range $M < a < (3\sqrt{3}/4)M$ and for $r > \hat{r}_+$ and $0 < r < \hat{r}_-$.
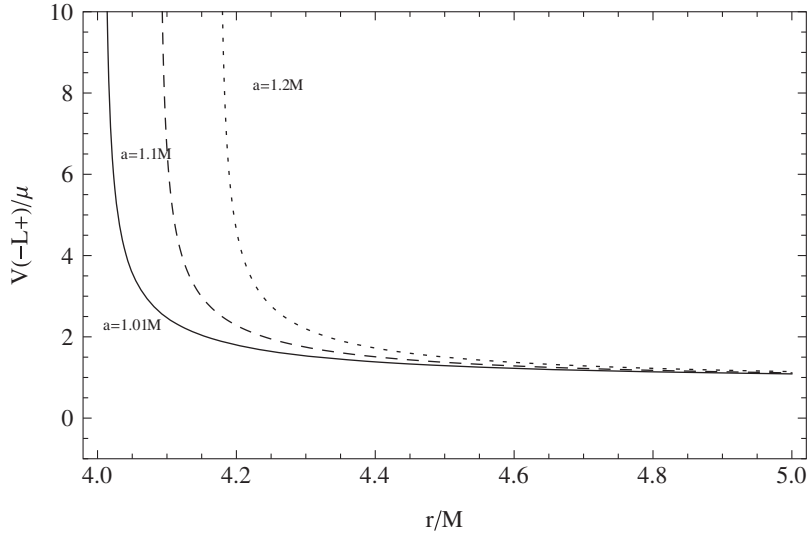
FIG. 29. The energy $E(-L_+)$ is plotted for selected values of a in the range $M < a < (3\sqrt{3}/4)M$ and for $r > r_a$. The energy $E(-L_+)$ is always strictly positive and increases as the angular momentum a/M increases.
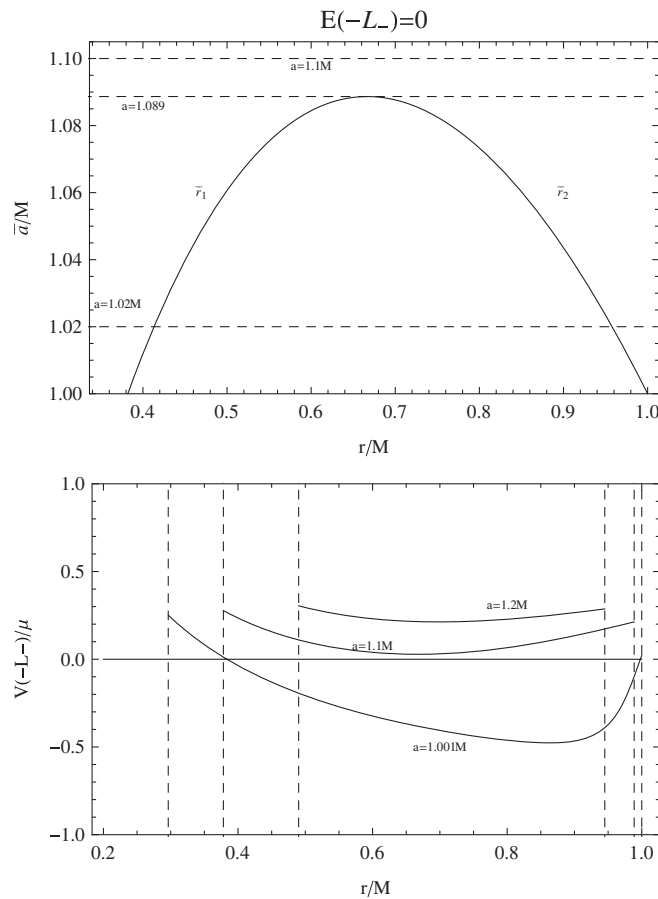

FIG. 30. The angular momentum $\bar{a} = -(r - 2M)\sqrt{r/M}$ is plotted as a function of r. The energy vanishes, $E(-L_-) = 0$, for $a = \bar{a}$, and is negative, $E(-L_-) < 0$, for $1 < a < \sqrt{32/27}M$ in the interval $\bar{r}_1 < r < \bar{r}_2$. For $a > \sqrt{32/27}M$ the energy $E(-L_-)$ is always strictly positive. For a naked singularity with momentum $a = 1.02M$ the energy $E(-L_-) = 0$ at $r = 0.41M$ and $r = 0.96M$, and $E(-L_-) < 0$ in $0.41M < r < 0.96M$. For $a = \sqrt{32/27}M$ the energy $E(-L_-) = 0$ at $r = 2/3M$, whereas $E(-L_-) > 0$ for $a = 1.1M$. In the bottom plot, the energy $E(-L_-)$ is plotted for selected values of a/M in the interval $\hat{r}_- < r < \hat{r}_+$.
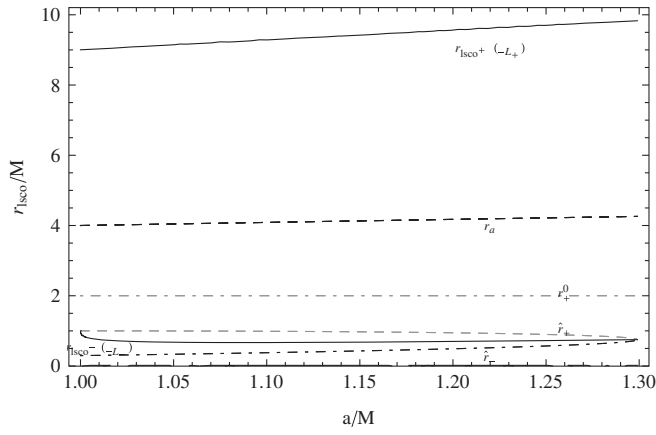
FIG. 31. The radii $r_{\text{lsco}}^{\pm}$ of the last stable circular orbits are plotted as functions of the intrinsic angular momentum a in the interval $M < a < \frac{3\sqrt{3}}{4}M$. The radii r_a and $\hat{r}_{\pm}$ are also plotted. The particle angular momentum $L_{\pm}$ is also denoted for some particular radii.

(v) In the region $r_a < r < r_{\text{lsco}}^{+}$, the orbits with $L = -L_+$ are unstable and those with $L = L_-$ are stable.

(vi) In the region $r > r_{\text{lsco}}^{+}$, the orbits with $L = -L_+$ and $L = L_-$ are stable.

The summary of this case is sketched in Fig. 32. As a concrete example, we investigate in detail circular motion around a naked singularity with $a = 1.1M$. The radii that determine the distribution of test particles in this gravitational field are $\hat{r}_{-} \approx 0.378M$, $\tilde{r}_{\text{lsco}}^{-} \approx 0.989M$, $\hat{r}_{+} = \approx 0.989M$, $r_a \approx 4.088M$, and $r_{\text{lsco}}^{+} = \approx 9.280M$. In Fig. 33, we illustrate the behavior of the angular momentum and the energy of circular orbits for this special case.

In Fig. 34, we show the behavior of the effective potential for some selected values of the orbital angular
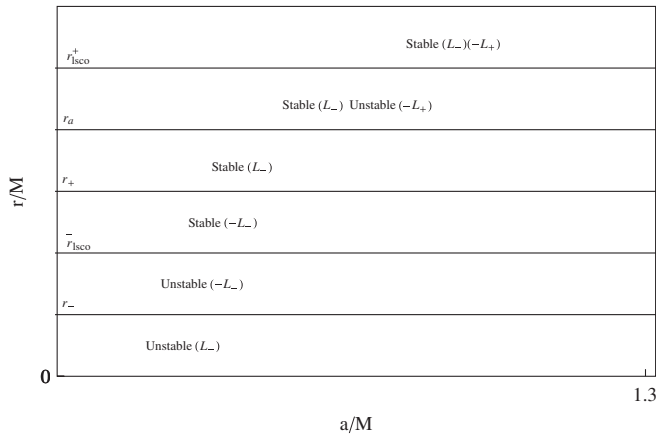

FIG. 32. Stability of circular orbits in a Kerr naked singularity with $M < a < \frac{3\sqrt{3}}{4}M$. The radii r_{lsco}^{+} and $\tilde{r}_{\text{lsco}}^{-}$ of the last stable circular orbits as functions of the ratio a/M. The special radii r_a and $\hat{r}_{\pm}$ are also plotted.

momentum. The turning points of the effective potential are located at $r_{\text{lsco}}^{+} \approx 9.280M$, where $L_{\text{lsco}}^{+} \approx -4.298\mu M$ and $V_{\text{lsco}}^{+} \approx 0.963\mu$, and at $\tilde{r}_{\text{lsco}}^{-} \approx 0.667M$, where $L_{\text{lsco}}^{-} \approx -0.354\mu M$ and $V_{\text{lsco}}^{-} \approx 0.028\mu$.

The essential results of our analysis can be described by using the model of an accretion disk around the central naked singularity. Considering the properties and positions of the different radii and the positions of the last stable circular orbits, we conclude that the stable accretion disk is composed of three different disks. The internal disk is situated between the radii $\tilde{r}_{\text{lsco}}^{-}$ and $\hat{r}_{+}$ and is made of stable particles of counterrotating particles with angular momentum $L = -L_-$. Particles situated on the boundary radius $\hat{r}_{+}$ turn out to be characterized by a zero value of the angular momentum (cf. Sec. IV C). A second disk made of stable corotating particles with angular momentum $L = L_-$ is situated in the region $\hat{r}_{+} < r < r_{\text{lsco}}^{+}$. Finally, the exterior stable disk is situated in the region $r > r_{\text{lsco}}^{+}$ and contains corotating particles with $L = L_-$ and counterrotating particles with $L = -L_+$.

C. Orbits with zero angular momentum

An interesting phenomenon that occurs only in the gravitational field of naked singularity is the existence of "circular orbits" with zero angular momentum, as defined by the conditions

$$V = E/\mu, \qquad V'(r) = 0, \qquad L = 0. \qquad (44)$$

This fact can be interpreted as a consequence of the repulsive gravity effects that characterize the dynamics in the field of the naked singularity. For the repulsive gravity effects in the Kerr spacetime see, for example, [39,40]. From the expression for the angular momentum derived in Sec. II one can show that the solution (44) is allowed only for naked singularities with intrinsic angular momentum within the interval $1 < a/M \leq 3\sqrt{3}/4$. Outside this interval, i.e., for $a/M > 3\sqrt{3}/4$, no orbits exist with zero angular momentum. The behavior of the corresponding effective potential is illustrated in Fig. 35.

A further analysis shows that the particles with $L = 0$ are situated on the radii $\hat{r}_{\pm}$, and that the radius $\hat{r}_{-}$ corresponds to unstable particles while the radius $\hat{r}_{+}$ is within the region of stability. This situation is illustrated in Fig. 36.

The analysis of the energy of test particles with $L = 0$ is presented in Fig. 37. For the stable particles that are situated on the radius $\hat{r}_{+}$ we can note that the energy is always positive and finite. The maximum value of the energy is reached at the ratio $a/M = 3\sqrt{3}/4$ and the minimum value with $E(\hat{r}_{+}) \to 0$ corresponds to the limit of the extreme black hole $a/M \to 1$.
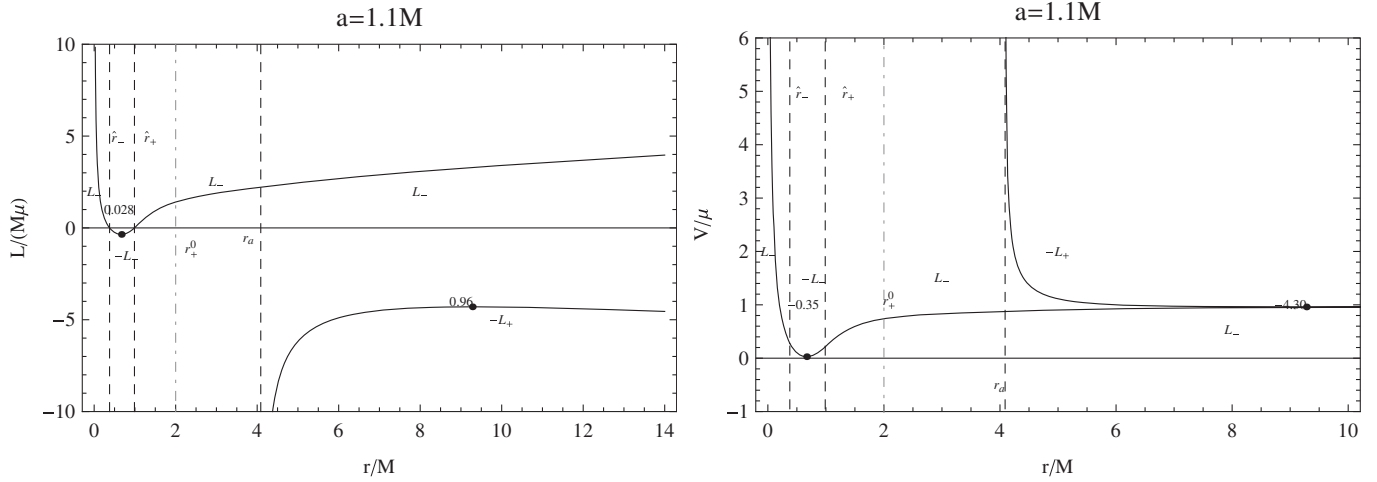
FIG. 33. Angular momentum and energy of circular orbits in a Kerr naked singularity with $a = 1.1M$. The dots denote the position of the last stable circular orbits, and the numbers close to the dots indicate the value of the energy V/μ or the angular momentum of the last stable circular orbits. In $r > r_a \approx 4.088M$, the particles have angular momentum $L = -L_+$; in $0 < r < \hat{r}_- \approx 0.378M$ and $r \geq \hat{r}_+ \approx 0.989M$, there exist particles with $L = L_-$; in $\hat{r}_- < r < \hat{r}_+$, there exist particles with $L = -L_-$.
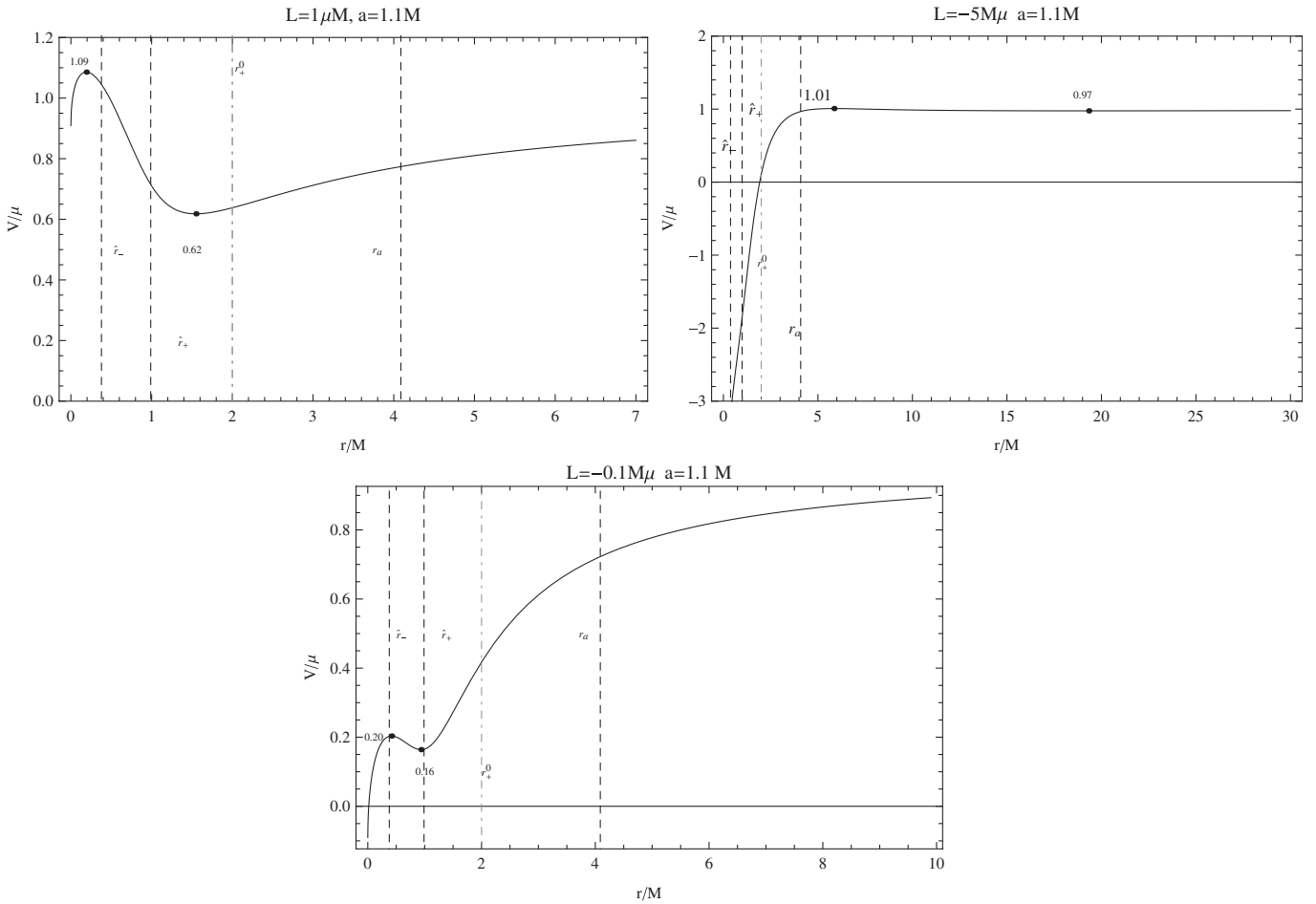

FIG. 34. The effective potential of a naked singularity with $a = 1.1M$ for fixed values of the particle angular momentum $L/(M\mu)$. The radii r_a and $\hat{r}_\pm$ are also plotted. The dots denote the critical points of the potential. Numbers close to the dots indicate the energy V/μ of the maxima and minima of the effective potential. The dash-dotted gray line represents the outer boundary of the ergosphere $r_+^0 = 2M$.
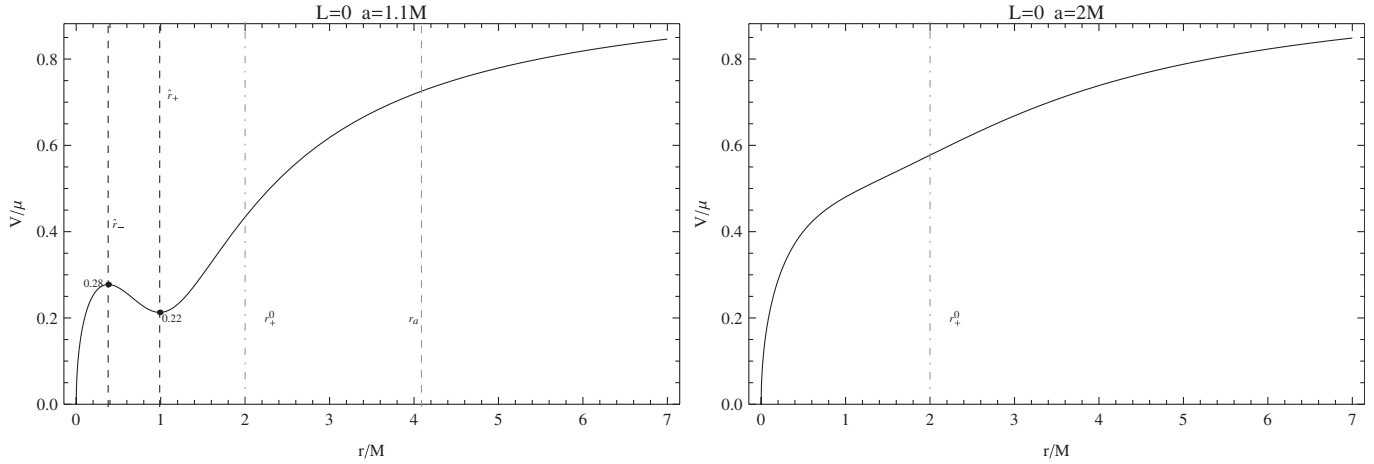
FIG. 35.   The effective potential of a Kerr naked singularity with angular momentum parameter $a = 1.1M$ and $a = 2M$ is plotted for the particle orbital angular momentum $L/(M\mu) = 0$ as a function of the radius r/M. The radii r_a and $\hat{r}_{\pm}$ are also plotted for both cases (see text). The dots represent the critical points of the potential, and the numbers close to the dots indicate the energy V/μ of the maxima and minima of the effective potential. In the case $a = 2M$ no extreme points are observed in the potential.

D. Summary of the naked singularity and black hole cases

In the investigation of the circular motion of test particles around a Kerr naked singularity we found that it is necessary to analyze separately the two regions $a \geq \frac{3\sqrt{3}}{4}M$ and $M < a < \frac{3\sqrt{3}}{4}M$. The distribution of orbits depends on the position of the special radii $\hat{r}_{\pm}$, given by Eq. (37), r_a, given by Eq. (33), and the position of the last stable circular orbits r_{lsco}^+, as given in Eq. (28), $\tilde{r}_{\text{lsco}}^-$ as given in Eq. (43), and $\bar{r}_{\text{lsco}}$, as given in Eq. (34). Notice that although the radius $\bar{r}_{\text{lsco}}$ is the geometric continuation of the radius $\tilde{r}_{\text{lsco}}^-$

for the interval $a/M > 3\sqrt{3}/4$, their values are determined by different analytical expressions as follows from Eqs. (28) and (34). The arrangement of these radii in the interval $1 < a/M < 1.7$ is depicted in Fig. 38.

Tables II and III summarize the distribution and stability properties of test particles in circular motion in the field of a rotating naked singularity for the two different regions of values of the intrinsic angular momentum.

For the sake of completeness, we show in Fig. 39 the behavior of the energies $E_{\text{lsco}}^+ = E(r_{\text{lsco}}^+)$ and $E_{\text{lsco}}^- = E(r_{\text{lsco}}^-)$ and angular momenta $L_{\text{lsco}}^+ = L(r_{\text{lsco}}^+)$ and $L_{\text{lsco}}^- = L(r_{\text{lsco}}^-)$, for the last stable circular orbits in terms of the
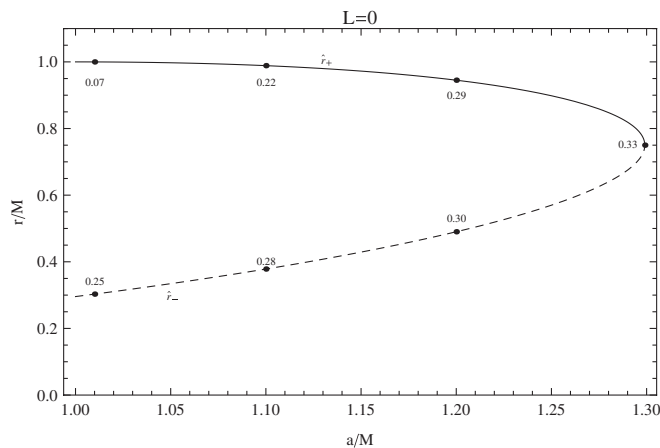

FIG. 36.   Location of particles with $L = 0$ in a Kerr naked singularity with $1 < a/M \leq 3\sqrt{3}/4$. The picture plots the locus of the critical points of the effective potential V/μ with (particle) angular momentum $L/(M\mu) = 0$. The radius of these "circular" orbits is plotted as a function of the source angular momentum a/M. Numbers close to the dots indicate the value of the energy V/μ.
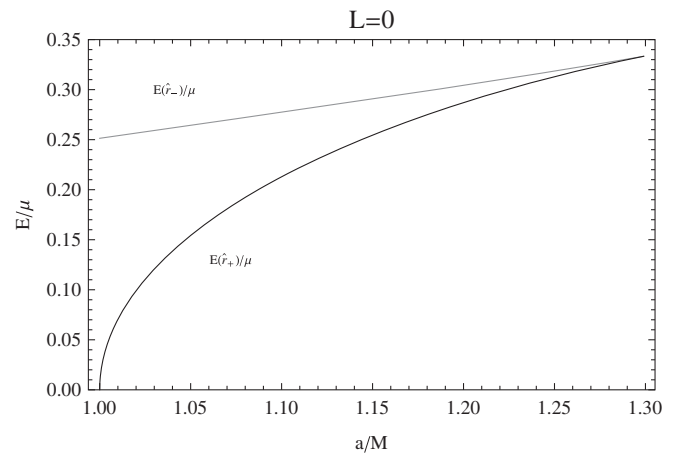
FIG. 37.   The energy particles with $L = 0$ in a naked singularity with $1 < a/M \leq 3\sqrt{3}/4$. The orbits are located on the radii $r = \hat{r}_+$ (stable) and $r = \hat{r}_-$ (unstable). The energies $E(\hat{r}_+)$ (solid black curve) and $E(\hat{r}_-)$ (solid gray curve) are plotted as functions of the intrinsic angular momentum a/M. It is possible to see that $E(\hat{r}_+) < E(\hat{r}_-)$ for $1 < a/M < 3\sqrt{3}/4$, and $E(\hat{r}_+) = E(\hat{r}_-)$ for $a/M = 3\sqrt{3}/4$.
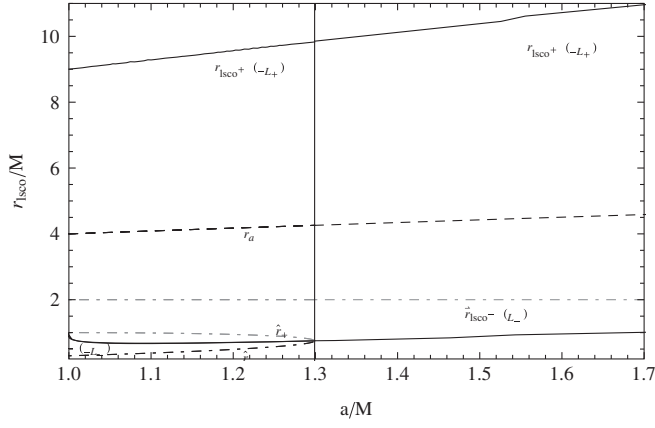
FIG. 38. The radii $r_{\rm lsco}$ of the turning points of the effective potential and the special radii r_a and $\hat{r}_\pm$ are plotted as functions of the ratio a/M within the interval [1, 1.7]. The dash-dotted gray line represents the outer boundary of the ergosphere $r_+^0 = 2M$.

TABLE II. Distribution and stability properties of circular orbits for a test particle in a Kerr naked singularity with $M < a < (3\sqrt{3}/4)M$. For each region we present the value of the orbital angular momentum of the particle as determined by Eq. (15).

Case: $M < a < (3\sqrt{3}/4)M$		
Region	Angular momentum	Stability
$]0, \hat{r}_-[$	L_-	$\tilde{r}_{\rm lsco}$
$]\hat{r}_-, \hat{r}_+[$	$-L_-$	$\tilde{r}_{\rm lsco}$
$]\hat{r}_+, \infty[$	L_-	$\tilde{r}_{\rm lsco}$
$]r_a, \infty[$	$-L_+$	$r_{\rm lsco}^+$
$]0, \hat{r}_-[$	L_-	Unstable
$]\hat{r}_-, \tilde{r}_{\rm lsco}[$	$-L_-$	Unstable
$]\tilde{r}_{\rm lsco}, \hat{r}_+[$	$-L_-$	Stable
$]\hat{r}_+, r_a[$	L_-	Stable
$]r_a, r_{\rm lsco}^+[$	$L_-(-L_+)$	Stable (Unstable)
$]r_{\rm lsco}^+, \infty[$	$(L_-, -L_+)$	Stable

ratio a/M of the naked singularity. Notice that, as expected from a physical viewpoint, for a fixed value of the ratio a/M the energy of the exterior last stable circular orbit $E(r_{\rm lsco}^+)$ is always smaller than the corresponding energy of the interior particle $E(r_{\rm lsco}^-)$.

Our analysis of Kerr black holes and naked singularities shows that the properties of circular orbits depend strongly on their radial distance with respect to the central source. The critical radii that are found in the analysis of the conditions for circular motion determine the angular momentum and the energy of the test particles. The arrangement of those special radii and the positions of the last stable circular orbits is depicted in Fig. 40 for the relevant ranges of the ratio a/M.

The radii r_a, r_γ, $\hat{r}_+$, and $\hat{r}_-$ determine the angular momentum and direction of rotation of test particles at a given distance from the central source. In addition, the radii $r_{\rm lsco}^\pm$ determine the position of the last stable circular orbits with a given angular momentum of the test particle.

If we imagine an infinitesimal thin disk made of test particles in circular orbits around the central compact object, the above results show that the geometric structure of the disk is sufficient to distinguish between black holes and naked singularities. For such a hypothetical disk to be a meaningful approximation of a physically realizable disk, it is necessary that the individual particle orbits be stable with respect to infinitesimal perturbations. In the case of radial perturbations, stability is guaranteed as a consequence of the fact that the disk is made of stable particles in circular motion, as described above. As for perturbations out of the equatorial plane, the analysis of stability has been performed by using the geodesic equations [41], the phase space method [42], and the Rayleigh criterion [43,44]. Although the last method has been applied only to static central sources, the generalization

TABLE III. Distribution and stability properties of circular orbits for a test particle in a Kerr naked singularity with $a \geq (3\sqrt{3}/4)M$. For each region we present the value of the orbital angular momentum of the particle as determined by Eq. (15).

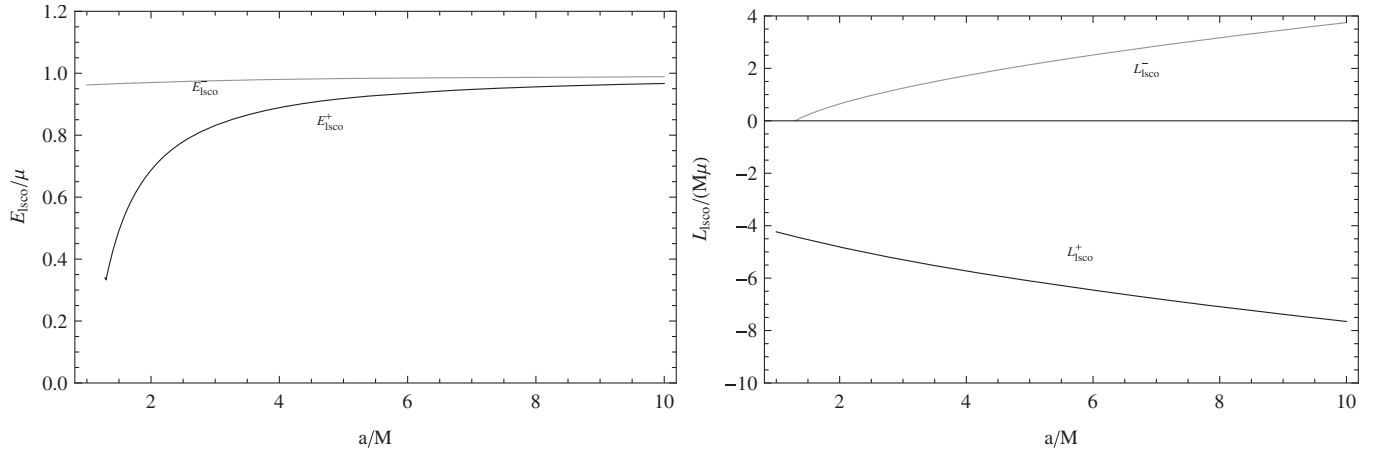| Case: $a \geq (3\sqrt{3}/4)M$		
Region	Angular momentum	Stability
$]0, \infty[$	L_-	$\bar{r}_{\rm lsco}$
$]r_a, \infty[$	$-L_+$	$r_{\rm lsco}^+$
$(3\sqrt{3}/4)M < a < 9M(\bar{r}_{\rm lsco} < r_a < r_{\rm lsco}^+)$		
$]0, \bar{r}_{\rm lsco}[$	L_-	Unstable
$]\bar{r}_{\rm lsco}, r_a[$	L_-	Stable
$]r_a, r_{\rm lsco}^+[$	$L_-(-L_+)$	Stable (Unstable)
$]r_{\rm lsco}^+, \infty[$	$(L_-, -L_+)$	Stable
$a \geq 9M(r_a < \bar{r}_{\rm lsco} < r_{\rm lsco}^+)$		
$]0, r_a[$	L_-	Unstable
$]r_a, \bar{r}_{\rm lsco}[$	$(L_-, -L_+)$	Unstable
$]\bar{r}_{\rm lsco}, r_{\rm lsco}^+[$	$L_-(-L_+)$	Stable (Unstable)
$]r_{\rm lsco}^+, \infty[$	$(L_-, -L_+)$	Stable

FIG. 39.   Behavior of the E_{lsco}/μ and the angular momentum for the last stable circular orbits as functions of the intrinsic angular momentum of the naked singularity.
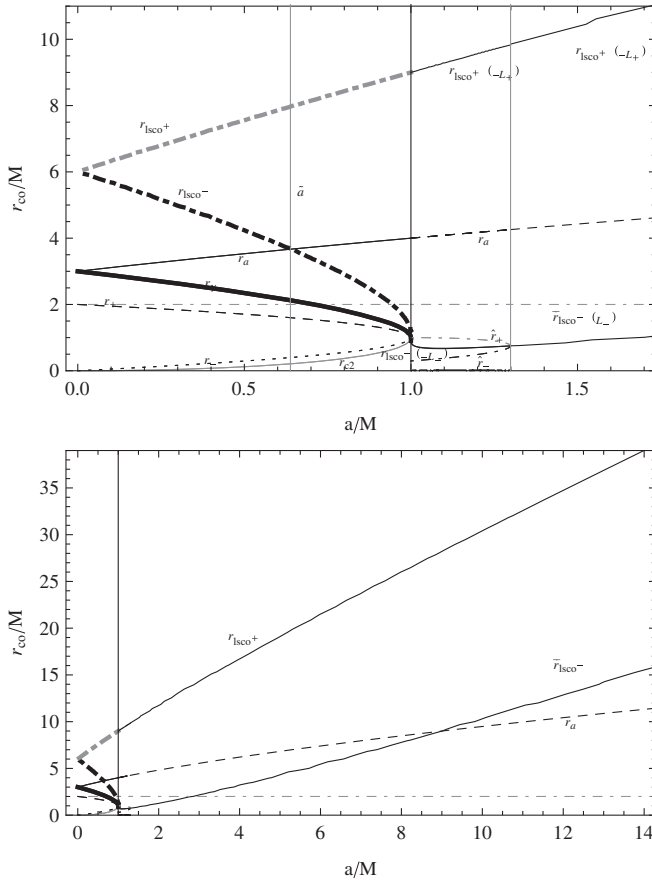

FIG. 40.   Arrangement of the radii determining the properties of circular orbits around a rotating central mass. The upper plot is for black holes and naked singularities with intrinsic angular momentum $a/M \in [0, 1.7]$. The bottom plot is for rotating naked singularities with $a/M \in [1.7, 14]$. The dash-dotted gray line represents the outer boundary of the ergosphere $r_+^0 = 2M$.

to include rotating sources seems to be straightforward. All those methods show that equatorial circular orbits around a Kerr black hole are stable under out-of-equatorial-plane perturbations as long as the angular momentum per unit mass of the test particles increases monotonically as the distance to the axis of symmetry increases. A complementary analysis must be performed in the case of naked singularities; however, a brief inspection of the analytical results obtained by using the phase space method seems to indicate that the stability does not depend drastically on the mass-to-angular-momentum ratio of the central body. In general, one can expect that the stability with respect to radial and out-of-equatorial-plane perturbations depends on the ratio of source rotation to particle angular momentum.

V. CONCLUSIONS

In this work, we investigated the circular motion of test particles around a rotating central mass whose gravitational field is described by the Kerr spacetime. We limit ourselves to the study of circular orbits situated on the equatorial plane $\theta = \pi/2$. First, we derive the conditions for the existence of circular orbits by using the fact the geodesic motion in this case can be reduced to the motion of test particles in an effective potential. In this procedure, two constants of motion arise, E and L, which are interpreted as the energy and the angular momentum of the test particles, respectively. We concentrate on the analysis of the conditions for the existence of circular orbits and their consequences for the values of the energy and angular momentum of the test particles. Our analysis covers completely the range of values of the intrinsic angular momentum of the central mass, including black holes and naked singularities. We find all the regions of the equatorial plane where circular motion is allowed and analyze the behavior of the energy

and the angular momentum of the test particles in those regions. Moreover, the stability properties of all the allowed circular orbits were investigated in detail.

For our analysis we consider separately the case of black holes with ratio $a/M \leq 1$ and naked singularities $a/M > 1$, where M is the mass and a is the specific angular momentum J/M of the central body. Moreover, in the case of naked singularities it turns out that the physical properties of the circular motion depend on the value of the ratio a/M so that it is necessary to explore two different ranges: $1 < a/M < 3\sqrt{3}/4$ and $a/M > 3\sqrt{3}/4$. The essential part of our results can be formulated in a plausible manner by using the model of an accretion disk made of stable test particles which are rotating around the central mass.

In the case of a black hole ($a/M \leq 1$), we find that the accretion disk is composed of an interior disk situated within the radii $[r_{\text{lsco}}^-, r_{\text{lsco}}^+]$ and an exterior disk in the region $r > r_{\text{lsco}}^+$, where $r_{\text{lsco}}^{\pm}$ represent the radius of the last stable circular orbit with angular momentum $L = \mp L_{\pm}$; moreover, the value of $L_{\pm}$ depends on the radius r of the circular orbit and on the ratio a/M of the central body [cf. Eq. (15)]. A similar accretion disk is found around naked singularities with $a/M > 3\sqrt{3}/4$. The only difference is that in the case of a naked singularity the interior disk, situated within the radii $[\bar{r}_{\text{lsco}}^-, r_{\text{lsco}}^+]$, has a minimum size of $r_{\text{lsco}}^+ - \bar{r}_{\text{lsco}}^- > 8M$, whereas in the case of a black hole the size of the inner disk is always less than $8M$ and disappears as $a \to 0$.

For naked singularities in the range $1 < a/M \leq 3\sqrt{3}/4$ we find that the stable accretion disk is composed of three different disks. The internal disk is situated between the radii $\tilde{r}_{\text{lsco}}^-$ and $\hat{r}_+ < r_{\text{lsco}}^+$ and is made of stable counter-rotating particles with angular momentum $L = -L_-$. The radius $\hat{r}_+$ corresponds to circular orbits with zero angular momentum $[V = E/\mu, V'(r) = 0, L = 0]$. A second disk made of stable corotating particles with angular momentum $L = L_-$ is situated in the region $\hat{r}_+ < r < r_{\text{lsco}}^+$. Finally, the exterior stable disk is situated in the region $r > r_{\text{lsco}}^+$ and contains corotating particles with $L = L_-$ and counterrotating particles with $L = -L_+$. We conclude

that the main difference between a rotating black hole and a rotating naked singularity consists in the different geometric structure of their accretion disks.

The study of the dynamics of test particles around compact rotating objects is surely interesting from the point of view of the astrophysical phenomenology. However, an immediate application of this study will be in the physics of the accretion disks as observed around astrophysical rotating objects (see [45–47] and also [39,48–50]; for the problem concerning the extended theories of gravity see, for example, [51]). The matter constituents, plasma elements, are the material of the electromagnetic jets as seen in the x-ray and γ-ray emissions. In this respect, a detailed and proper description of the test particle dynamics is the first step towards the construction of a realistic model for accretion disks around Kerr sources (see [39,52–54], and also [55,56]).

In this work, we also explored the physics of naked singularities (see also [10–12,57]). As no naked singularity has been yet observed and furthermore the existence of these objects is still a subject under intensive theoretical debate, the analysis of the dynamical properties of these objects is clearly important either for a formalization of a complete theoretical picture of the physical features of these solutions or for observational issues [58–63] (see also [64,65]). We expect to generalize this work to include the physical contribution of a charged source, therefore, exploring the Kerr-Newman metric which properly describes the spacetime of a rotating, electrically charged, compact object in general relativity [14].

[1] S. Chandrasekhar, *The Mathematical Theory of Black Holes* (Oxford University Press, New York, 1983).
[2] D. J. Raine and E. Thomas, *Black Holes: An Introduction* (London, Imperial College Press, 2010).
[3] M. P. Hobson, G. P. Efstathiou, and A. N. Lasenby, *General Relativity: An Introduction for Physicists* (Cambridge University Press, Cambridge, England, 2006).
[4] J. M. Bardeen, Nature (London) **226**, 64 (1970).
[5] J. M. Bardeen, W. H. Press, and S. A. Teukolsky, Astrophys. J. **178**, 347 (1972).
[6] I. Bredberg, C. Keeler, V. Lysov, and A. Strominger, arXiv:1103.2355.
[7] Z. Stuchlik, Bull. Astron. Inst. Czech. **31**, 129 (1980).
[8] C. Misner, K. Thorne, and J. Wheeler, *Gravitation* (Freemann and Company, San Francisco, 1973).
[9] R. Ruffini, in *Black Holes—Les Astres Occlus*, edited by C. DeWitt and B. S. DeWitt (Gordon and Breach, New York, 1973).
[10] D. Pugliese, H. Quevedo, and R. Ruffini, arXiv:1003.2687.
[11] D. Pugliese, H. Quevedo, and R. Ruffini, Phys. Rev. D **83**, 024021 (2011).

[12] D. Pugliese, H. Quevedo, and R. Ruffini, Phys. Rev. D **83**, 104052 (2011).

[13] S. Chandrasekhar, *Principles of Stellar Dynamics* (Dover Publications, New York, 1942).

[14] V. Balek, J. Bicak, and Z. Stuchlik, Bull. Astron. Inst. Czech. **40**, 133 (1989).

[15] D. Bini and R. T. Jantzen, Classical Quantum Gravity **17**, 1637 (2000).

[16] P. G. Komorowski, S. R. Valluri, and M. Houde, Classical Quantum Gravity **26**, 085 001 (2009).

[17] P. G. Komorowski, S. R. Valluri, and M. Houde, Classical Quantum Gravity **27**, 225 023 (2010).

[18] P. G. Komorowski, S. R. Valluri, and M. Houde, arXiv:1101.0996.

[19] E. Hackmann, V. Kagramanova, J. Kunz, and C. Lammerzahl, Europhys. Lett. **88**, 30 008 (2009).

[20] M. Favata, Phys. Rev. D **83**, 024028 (2011).

[21] D. Bini, C. Cherubini, G. Cruciani, and R. T. Jantzen, Int. J. Mod. Phys. D **13**, 1771 (2004).

[22] D. Bini, P. Carini, and R. T. Jantzen, Int. J. Mod. Phys. D **6**, 143 (1997).

[23] D. Bini, C. Cherubini, A. Geralico, and R. T. Jantzen, Gen. Relativ. Gravit. **40**, 985 (2008).

[24] F. De Felice and M. Calvani, Nuovo Cimento Soc. Ital. Fis. **10B**, 447 (1972).

[25] F. De Felice, Phys. Rev. D **19**, 451 (1979).

[26] J. Gariel, M. A. H. MacCallum, G. Marcilhacy, and N. O. Santos, arXiv:gr-qc/0702123 [Astron. Astrophys. (to be published)].

[27] C. Chicone and B. Mashhoon, Classical Quantum Gravity **23**, 4021 (2006).

[28] K. Lake, Phys. Rev. Lett. **104**, 211102 (2010); **104**, 259903(E) (2010).

[29] E. Hackmann, C. Lammerzahl, V. Kagramanova, and J. Kunz, Phys. Rev. D **81**, 044020 (2010).

[30] D. Bini, F. de Felice, and A. Geralico, Classical Quantum Gravity **21**, 5427 (2004).

[31] D. Bini, F. de Felice, and A. Geralico, Classical Quantum Gravity **21**, 5441 (2004).

[32] D. Bini, A. Geralico, and R. T. Jantzen, Classical Quantum Gravity **22**, 4729 (2005).

[33] D. Bini, A. Geralico, R. T. Jantzen, and F. de Felice, Classical Quantum Gravity **23**, 3287 (2006).

[34] V. I. Dokuchaev, arXiv:1103.6140.

[35] S. Suzuki and K. Maeda, Phys. Rev. D **58**, 023005 (1998).

[36] G. A. Gonzalez and F. Lopez-Suspes, arXiv:1104.0346.

[37] P. Pani, E. Barausse, E. Berti, and V. Cardoso, Phys. Rev. D **82**, 044009 (2010).

[38] D. Grumiller and A. M. Piso, arXiv:0909.2041.

[39] F. de Felice and M. Bradley, Classical Quantum Gravity **5**, 1577 (1988).

[40] G. Preti and F. de Felice, Am. J. Phys. **76**, 671 (2008).

[41] J. M. Bardeen, Astrophys. J. **161**, 103 (1970).

[42] A. Palit, A. Pachenko, N. G. Migranov, A. Bhadra, and K. K. Nandi, Int. J. Theor. Phys. **48**, 1271 (2008).

[43] P. S. Letelier, Phys. Rev. D **68**, 104002 (2003).

[44] J. Ramos-Caro, J. F. Pedraza, and P. S. Letelier, Mon. Not. R. Astron. Soc. **414**, 3105 (2011).

[45] K. P. Tod, F. de Felice, and M. Calvani, Nuovo Cimento Soc. Ital. Fis. **34B**, 365 (1976).

[46] S. W. Wei, Y. X. Liu, H. Guo, and C. E. Fu, Phys. Rev. D **82**, 103005 (2010).

[47] A. A. Grib and Y. V. Pavlov, arXiv:1007.3222.

[48] D. Bini, A. Geralico, O. Luongo, and H. Quevedo, Classical Quantum Gravity **26**, 225 006 (2009).

[49] T. Harada and M. Kimura, Phys. Rev. D **83**, 024002 (2011).

[50] T. Harada and M. Kimura, Phys. Rev. D **83**, 084041 (2011).

[51] S. Capozziello, M. De laurentis, and A. Stabile, Classical Quantum Gravity **27**, 165 008 (2010).

[52] T. Ledvinka, M. Zofka, and J. Bicak, arXiv:gr-qc/9801053.

[53] C. Bambi and N. Yoshida, Phys. Rev. D **82**, 124037 (2010).

[54] V. Zhuravlev and P. Ivanov, arXiv:1103.5739 [Mon. Not. R. Astron. Soc. (to be published)].

[55] D. R. Staicova and P. P. Fiziev, Astrophys. Space Sci. **332**, 385 (2010).

[56] F. Tamburini, B. Thide, G. Molina-Terriza, and G. Anzolin, Nature Phys. **7**, 195 (2011).

[57] F. de Felice, Nuovo Cimento Soc. Ital. Fis. **122B**, 481 (2007).

[58] R. Penrose, Nuovo Cimento B **1**, 252 (1969); reprinted in Gen. Relativ. Gravit. **34**, 1141 (2002).

[59] S. W. Hawking and G. F. R. Ellis, *The Large Scale Structure of Space-Time* (Cambridge University Press, Cambridge, England, 1973).

[60] M. Patil and P. S. Joshi, arXiv:1103.1082.

[61] P. S. Joshi, D. Malafarina, and R. Narayan, arXiv:1106.5438.

[62] P. S. Joshi and D. Malafarina, arXiv:1105.4336.

[63] M. Patil and P. S. Joshi, arXiv:1103.1083.

[64] R. Di Criscienzo, L. Vanzo, and S. Zerbini, J. High Energy Phys. 05 (2010) 092.

[65] K. S. Virbhadra and C. R. Keeton, Phys. Rev. D **77**, 124014 (2008).